

Materials Science & Engineering B: Advanced Functional Solid-State Materials



ISSN: 0921-5107; Impact Factor: 4.706

Editor for Fluid Dynamics: Prof. S. Jin, Department of Mechanical and Aerospace Engineering, University of California San Diego, La Jolla, California, United States.

Accepted August 14th 2020.

NUMERICAL SIMULATION OF HYDROMAGNETIC MARANGONI CONVECTION FLOW IN A DARCIAN POROUS SEMICONDUCTOR MELT ENCLOSURE WITH BUOYANCY AND HEAT GENERATION EFFECTS

O. Anwar Bég^A, K. Venkatadri^B, V. Ramachandra Prasad^{*C}, T. A. Bég^D, A. Kadir^A and Henry J. Leonard^A

^A Multi-Physical Engineering Sciences Group, Aeronautical/Mechanical Engineering, Salford University, School of Science, Engineering and Environment (SEE), Manchester, M54WT, UK. E-Mail : O.A.Beg@salford.ac.uk ; Email: A.Kadir@salford.ac.uk
E-Mail : h.leonard@salford.ac.uk

^B Dept. Mathematics, Sreenivasa Institute of Technology/Management Studies, Chittoor, Andhra Pradesh, 517127, India.
E-Mail: venkatadri.venki@gmail.com

^C Dept. Mathematics, School of Advanced Sciences, Vellore Institute of Technology, Vellore – 6322014, India.
*rcpmaths@gmail.com

^D Engineering Mechanics Research, Israfil House, Dickenson Rd., Manchester, M13, UK.
E-Mail; tasveerabeg@gmail.com;

***Corresponding author. Email: rcpmaths@gmail.com**

ABSTRACT:

We present a mathematical and numerical study of the transient Marangoni thermo-convection flow of an electrically conducting Newtonian fluid in an isotropic Darcy porous rectangular semiconductor melt enclosure with buoyancy and internal heat generation effects, in an (x, y) coordinate system. The governing equations comprising the mass conservation, x -direction momentum, y -direction momentum and energy equation are formulated subject to a quartet of boundary conditions at the four walls of the enclosure. The upper enclosure wall is assumed to be “free” with an appropriate surface tension dynamic boundary condition. A series of transformations are implemented to render the mathematical model dimensionless and into a vorticity form. The governing thermophysical parameters are shown to be the Marangoni number for surface tension (thermocapillary) effects (Ma), Prandtl number (Pr), Grashof number for buoyancy effects (Gr), enclosure aspect ratio (A), Hartmann hydromagnetic number (Ha), Darcy number for bulk porous resistance (Da), and the internal heat generation parameter (I) the latter being a function of the internal (Ra_i) and global Rayleigh numbers (Ra). An efficient finite difference numerical method is employed to solve the boundary value problem. Validations with earlier purely fluid solutions ($Da \rightarrow \infty$) are included. A mesh-independence test is included with further validation with other published studies. Isotherms and isovels (streamlines) are computed as are Nusselt numbers at selected boundaries. Solutions for the case of $Pr = 0.054$ (semiconductor melt) are also compared with earlier studies showing excellent correlation. The model finds applications in the bulk crystal growth of semiconductors, electromagnetic materials processing control and also hybrid fuel cells.

KEY WORDS: *Marangoni Convection; Hydromagnetics; Porous Media; Darcy model; MAC computation; Heat Source; Semiconductor Melt; Buoyancy; Materials Processing.*

NOMENCLATURE

Dimensional

x	<i>co-ordinate parallel to base of enclosure (m)</i>
y	<i>co-ordinate perpendicular to base of enclosure (m)</i>
g	<i>acceleration due to gravity (m/s^2)</i>
H	<i>height of enclosure (m)</i>
L	<i>length of enclosure (m)</i>
\mathbf{B}	<i>uniform magnetic field vector (Tesla)</i>
u	<i>x-direction velocity (m/s)</i>
v	<i>y-direction velocity (m/s)</i>
B_0	<i>magnitude of \mathbf{B} (Tesla)</i>
K	<i>permeability of the porous medium (m^2)</i>
p	<i>hydrodynamic pressure (Pa)</i>
K	<i>effective thermal conductivity of fluid saturated porous medium (W/mK)</i>
t	<i>time (s)</i>
T	<i>temperature (K)</i>
C_p	<i>isobaric specific heat (J/kgK)</i>
J	<i>electrical current density (Amperes/m^2)</i>
\mathbf{V}	<i>field velocity vector (m/s)</i>
q'''	<i>volumetric internal heat generation rate (W/m^3)</i>
σ	<i>electrical conductivity of fluid (Siemens/m)</i>
β	<i>thermal expansion coefficient of fluid (/K)</i>
ϕ	<i>electric potential (Volts)</i>
μ	<i>dynamic viscosity of fluid (kg/ms)</i>
ν	<i>kinematic viscosity of fluid (m^2/s)</i>
ρ	<i>fluid density at reference temperature (kg/m^3)</i>
σ^*	<i>surface tension (N/m)</i>
γ	<i>temperature coefficient (/K)</i>
α	<i>thermal diffusivity of fluid-saturated porous medium (m^2/s)</i>
q	<i>heat flux (w/m^2)</i>

Dimensionless

τ	<i>dimensionless time</i>
Ha	<i>Hartmann hydromagnetic number</i>

Da	<i>Darcian porous number</i>
Ma	<i>Marangoni number</i>
Pr	<i>Prandtl number</i>
Nu	<i>Nusselt number</i>
Gr	<i>Grashof number</i>
Ra	<i>Rayleigh number</i>
Ra_i	<i>Internal Rayleigh number</i>
X	<i>dimensionless x co-ordinate</i>
Y	<i>dimensionless y co-ordinate</i>
U	<i>dimensionless u velocity</i>
V	<i>dimensionless v velocity</i>
θ	<i>dimensionless temperature</i>
A	<i>aspect ratio (L/H)</i>
ψ	<i>stream function</i>
Ω	<i>vorticity function</i>

Subscripts and Superscripts

$()_H$	<i>Hot wall (right of enclosure)</i>
$()_C$	<i>Cold wall (left of enclosure)</i>

1. INTRODUCTION

Natural convection flows in enclosures continue to attract the attention of engineers and scientists owing to the extensive applications of such studies in solar energy systems, crystal growth technologies, storage of hazardous materials in geo-repositories, materials processing, large fuel tanks etc [1]. In conjunction with experimentation, extensive computational studies of both natural convection and thermosolutal convection flows have been reported using a variety of numerical procedures for both Newtonian and non-newtonian fluids. Robillard *et al.* [2] investigated the heat transfer in a rectangular enclosure with a constant rate of cooling at the walls. Kwak and Hyun [3] considered the influence of side-wall transient temperature conditions on free convection in an enclosure using an unsteady finite difference model, showing that resonance is characterized by maximal amplification of the fluctuations of heat transfer in the interior and that resonance becomes more distinctive for large Rayleigh numbers when Prandtl number is of order unity.

Bennacer *et al.* [4] used a finite element method to investigate the unsteady free convection heat transfer in an enclosure with vertical mass transfer gradients. Welhezi *et al.* [5] deployed a second-order accurate finite volume approach on a staggered grid system and multi-grid acceleration to simulate the buoyancy-driven convection in a body of cubical shape located at the center of an isothermal cooled spherical enclosure, considering three different fluids (air, water and dielectric liquid). They noted that thermal and velocity fields eventually attain steady states when Rayleigh numbers range from 10^4 to 10^7 . Bhargava *et al.* [6] studied the double-diffusive convection in a square enclosure (as a model of a bioreactor) containing micropolar fluid. Using both variational finite element and optimized finite difference schemes and showing that microstructural parameters in combination with Lewis and Rayleigh numbers exert a profound influence on iso-temperature, iso-concentration and iso-microrotation distributions. More recently Kuharat *et al.* [7] employed finite volume ANSYS FLUENT software to compute the thermal performance of silver and titanium oxide-water nanofluids in rectangular solar collector enclosures for a variety of volume fractions and aspect ratios. These studies considered *purely fluid* cavities i.e. neglected permeable material presence and also assumed the circulating fluid to be *electrically non-conducting*. However, many industrial applications involving thermal convection in enclosures feature *porous media* and also magnetized fluids subjected to external *static or alternating magnetic fields*. Engineers have therefore also studied magnetohydrodynamic convection in enclosures with/without porous media. Gelfgat and Bar-Joseph [8] considered the influence of external magnetic field on oscillatory convective flows in a rectangular enclosure, as a simulation of Bridgman crystal growth processes. For Prandtl number of 0.015, they computed the influence of magnetic field at various inclinations on the stability of the two distinct branches (with a single-cell or a two-cell pattern) of the steady state flows, observing that a vertical magnetic field achieves the most effective stabilization. Bourantas and Loukopoulos [9] utilized a meshless point collocation method utilizing a velocity-correction scheme to analyze numerically the unsteady free convection magnetohydrodynamic micropolar-nanofluid ($\text{Al}_2\text{O}_3/\text{water}$) in an inclined rectangular enclosure is considered. They noted that velocity and temperature are generally strongly modified by strength and orientation of the magnetic field and temperatures elevated with nanoparticle volume fraction up to a critical point. Sheremet *et al.* [10] employed a second order finite difference method to analyse the hydromagnetic free convection in an inclined wavy Cu–water nanofluid enclosure featuring an isothermal corner heater. They presented average Nusselt number and isotherm plots for the influence of Hartmann magnetic number, magnetic field inclination, wavy boundary undulation number,

inclination angle of the cavity, solid volume fraction parameter of nanoparticles and dimensionless time. Wang *et al.* [11] studied the free convection in a porous cavity using the Darcian formulation. Amahmid *et al.* [12] analyzed the convective heat and mass transfer in a vertical porous Darcian enclosure. Zhang *et al.* [13] used a mixed finite element method comprising a Brezzi-Douglas-Marini element and a discontinuous Galerkin element to compute heat and mass transfer in a Darcian porous enclosure for CO₂ sequestration in brine aquifers. Stajnko *et al.* [14] employed a boundary domain integral method (BDIM), to compute convection heat transfer in an isotropic porous medium with the Darcy model and the velocity-vorticity formulation of the Navier-Stokes equations. Pekmen and Tezer-Sezgin [15] applied a dual reciprocity boundary element method (DRBEM) to compute the steady free magnetic convection in complex enclosures filled with a fluid saturated porous medium. They showed that stronger magnetic field and lower permeability damps the circulation and significantly alters conductive heat transfer. Magnetic field was therefore shown to be an effective mechanism of controlling heat transfer processes in porous media. Alchaar *et al.* [16] investigated the influence of transverse magnetic field on free convection in a rectangular porous enclosure. Alsabery *et al.* [17] used COMSOL finite element software to analyse the impact of viscous heating and radiation on MHD natural convection in an oblique porous cavity with constant heat flux. They noted that the intensity of the streamlines and the isotherm patterns is reduced with an increment in Hartmann magnetic number and permeability (Darcy number) and that heat transfer is boosted with viscous heating and radiative flux. Pekmen and Tezer-Sezgin [18] studied mixed convection flow in a lid-driven square cavity filled with a porous medium under the effect of a magnetic field with the dual reciprocity boundary element method (DRBEM) and a Houbolt time integration scheme, including the effect of magnetic induction. They showed that lower permeability of porous medium and greater applied magnetic field induces flow deceleration and suppresses convective heat transfer whereas intensification in magnetic potential circulating throughout the cavity with high magnetic permeability of the fluid is generated. Bég *et al.* [19] used network simulation PSPICE software to simulate the rotating magnetohydrodynamic Hall flow in a Darcian regime with oblique magnetic field, observing that decreasing Darcy number (lower permeability) strongly damps the velocity field and eliminates oscillatory instabilities. Bhatti *et al.* [20] used the successive linearization method to compute hydrodynamic wall slip and radiative heat flux effects on magnetic iron oxide-water-based nanofluid Sakiadis flow in a porous medium with cross diffusion effects. An excellent study of non-Darcy convection in an annular porous structure was presented by Muralidhar and Kulacki [21]. Shivakumara *et al.* [22] investigated the unsteady non-Darcian

free convection in a vertical cylindrical porous medium annulus using a finite difference method, showing that decreasing Darcy number suppresses velocity fields and also reduces boundary heat transfer rates. Khadrawi and Nimr [23] considered the transient hydrodynamics and buoyancy-driven heat transfer in an open-ended vertical parallel-plate channel partially filled with a non-Darcian porous medium. Further studies deploying a robust Forchheimer-extended Darcy model include Rawat *et al.* [24] on time-dependent magnetoconvective non-Newtonian thermosolutal convection in a non-Darcy porous medium channel with variable thermal conductivity and heat source effects. They employed a variational finite element code and showed that significant modification in both core flow and wall shear stress, Nusselt number and Sherwood numbers is caused with increment in Forchheimer parameter and transverse magnetic field strength, although flow reversal is avoided. Prasad *et al.* [25] used a second order finite difference method to simulate Soret and Dufour cross diffusion effects on enrobing thermosolutal boundary flow from a cylindrical body in Darcy-Forchheimer permeable media. Prasad *et al.* [26] further investigated thermophoresis and Brownian motion effects on Buongiorno nanofluid coating flow over a spherical geometry in non-Darcy porous media, computing general solutions and also stagnation point characteristics. Aly [27] used an incompressible smoothed particle hydrodynamics (ISPH) method to compute the non-Darcy natural convective heat and mass transfer in an enclosure saturated with anisotropic porous media with and without a sloshing rod inside the enclosure. He utilized a semi-implicit velocity correction procedure and presented streamlines, isotherms, concentration contours and average Nusselt and Sherwood numbers. These computations showed that increasing Darcy number, porosity, permeability ratio and inclination angle substantially alter wall heat and mass transfer characteristics. Bég *et al.* [28] used a Darcy–Forchheimer isotropic porous medium drag force model, the P1 radiative model and both forward time centered space (FTCS) finite difference and network thermoelectric simulation codes (RAD-SPACE) to compute the velocity, temperature and dimensionless zero moment of intensity distributions in the annular region of a hybrid solar collector enclosure. These simulations indicated that increasing aspect ratio and Darcy number accelerates axial and radial flow and enhances radiative moment of intensity, whereas increasing Forchheimer number decelerates the axial and radial flow. They further showed that greater radiative optical thickness of the saturated porous medium retards radial flow whereas it accelerates axial flow and accentuates temperatures.

In all the above studies either closed systems or boundary layer flows have been considered i.e. *they have not considered the influence of a free surface* on the convection regime.

However, when *free surfaces* are present in natural convection flows it has been shown that motion is induced in the fluid via *surface tension* at the free surface. It may also be induced by surfactant concentration gradients at the interface of two fluid layers which can produce interfacial flows from regions of low surface tension to region of high surface tension. Although discovered over a century ago, Marangoni flows continue to find novel applications in modern engineering sciences. These include ballistic phase spacecraft rocket fuel tank thermophysics [29], fuel flame spread in transient molten tin soldering processes [30], aircraft pool fires [31]. In electromagnetic materials processing, pulsed laser texturing [32] is employed in computer disk coating and exploits Marangoni convection. Owing to the highly localized melting pool, the high temperature gradients produced during the process require very judicious control and Marangoni convection effects dominate such regimes. Further applications of Marangoni convection flows arise in laser heating techniques [33], liquid metal processing [34] and floating zone micro-gravity flows in astronomical experiments [35]. Magnetohydrodynamic (MHD) Marangoni convection is of particular importance in Czochralski flows arising in semiconductor materials processing [36]. Marangoni MHD flows have therefore received considerable attention in recent years from a simulation perspective. Sastry *et al.* [37] computed the Marangoni hydromagnetic nanofluid flow from a plane surface using the the MATLAB “bvp4c” program, a surface tension boundary condition and considering various nanoparticles (Cu, Al₂O₃, and TiO₂) with water base fluid. Zueco and Bég [38] used electrothermal network simulation to study the magnetohydrodynamic Marangoni mixed convection boundary layer flow from a vertical plate. They showed that greater Hartmann hydromagnetic number damps the flow and elevates temperatures. Furthermore, they observed that increment in Marangoni mixed convection parameter in opposing Marangoni flow substantially boosts the flow whereas it depresses temperatures with the contrary behavior for assisting Marangoni flow. Zhang *et al.* [39] applied a double-parameter transformation perturbation expansion method and Padé approximants technique to derive solutions for reactive MHD thermosolutal Marangoni convection with heat source present, with a linear surface tension variation with both the temperature and concentration and an interface temperature and concentration being quadratic functions of the interface arc length. Bég *et al.* [40] computed the thermocapillary nanofluid magneto-convection from a non-isothermal surface with magnetic induction effects with Maple shooting quadrature for silver, copper, aluminium oxide and titanium oxide nanoparticles in aqueous base fluids using a Tiwari–Das model. They showed that magnetic stream function is strongly increased with magnetic field in the presence of significant Marangoni surface tension effect whereas the flow and magnetic

stream function gradient are suppressed with increasing nanofluid solid volume fraction, whereas temperatures are significantly enhanced. Lin *et al.* [41] studied the Marangoni convection heat transfer of an electrically conducting power-law fluid driven by temperature gradient, with linear surface tension variation and a modified Fourier law for power-law fluids. Several works focused on magnetic Marangoni convection in enclosures have also appeared. Ma *et al.* [42] investigated forced convection in liquid encapsulated Czochralski or Kyropoulos growth of compound semiconductor crystals under a uniform vertical magnetic field. They observed that electromagnetic damping of the forced convection exceeds that due to buoyant convection and an intricate interplay exists between magnetic body force, thermal buoyancy and Marangoni surface tension. Rudraiah *et al.* [43] presented a rigorous study of thermocapillary hydromagnetic convection in a square cavity using an ADI (Alternating Direction Implicit) method, with upwind differencing for non-linear convective terms and the SLOR (Successive Line Over Relaxation) algorithm. They showed that magnetic field dampens hydrodynamic oscillations and can increase the purity of crystals. Magnetic fields were shown to effectively regulate the heat transfer rates and stabilize flows in semiconductor crystal growth. Oscillatory instability can have a damaging influence on crystal development and magnetic fields have been shown to enhance compositional uniformity and minimize defect density in these and other studies. Chippada *et al.* [44] studied the buoyancy driven Marangoni convection in open cavities using the Chorin time-splitting scheme. The influence of Marangoni number, Bond number, Ohnesorge number, Prandtl number and Grashof number on the flow regime was computed. Saghir *et al.* [45] presented a detailed study of Rayleigh-Marangoni convection in a Darcian porous medium cavity. They computed flow patterns for Darcy number of 9×10^{-6} and for a porosity of 0.39, for n-Hexane fluid using the finite element method. A finer numerical grid was implemented near the free surface where Marangoni effects are maximized. Marangoni convection was shown to induce a breakaway of the convection rolls generating four cells in the square cavity of different sizes and directions. Convection was thereby enhanced in the porous cavity and hexagonal patterns were identified. Juel *et al.* [46] studied hydromagnetic Marangoni convection in an enclosure filled with molten Gallium. Saleem *et al.* [47] simulated thermosolutal reactive Marangoni magneto-convection flow in a square cavity under inclined magnetic field using an alternate direct implicit (ADI) method. They noted that average Nusselt number is reduced whereas the average Sherwood number is elevated with greater orientation of magnetic field from the horizontal to vertical positions. They also found that thermal buoyancy exerts a weaker influence on circulation relative to solutal buoyancy effect. Hossain *et al.* [48] used an upwind finite difference code with a SOR

technique to study the transient laminar natural magnetohydrodynamic Marangoni convection flow in a rectangular enclosure with internal heat source for Prandtl number of 0.054 (semiconductor melt). They showed that modification in direction of the external magnetic force from horizontal to vertical reduces flow rates in both the primary and the secondary cells and increases the impact of the thermocapillary (Marangoni) effect. They also showed that greater heat generation multiplies significantly the number of vortex cells in the enclosure.

The above studies did not simultaneously consider magnetohydrodynamics, Marangoni and Darcian porous media effects. This is the objective of the present study wherein a novel model is developed to simulate the composite effects of buoyancy, magnetic field, Darcian bulk resistance and internal heat generation and oblique magnetic field on Marangoni convection flow in a rectangular enclosure containing an isotropic porous medium. The Darcy formulation has been employed earlier by Bég *et al.* [49], Bég and Makinde [50], and Bég *et al.* [51]. A robust marker and cell (MAC) numerical code [52] is implemented to solve the vorticity form of the conservation equations and to compute flow regime isotherms and stream-function patterns. Verification of the computations is conducted with the purely fluid solutions of Hossain *et al.* [48]. Such a study constitutes an important extension to the literature on semiconductor melt convection in porous enclosures and has not been communicated thus far in the technical literature. **The advantage and the disadvantage of the free layer assumption addressed by [63].** It is also important in chemical engineering control technologies and hybrid green fuel cell applications.

2. MATHEMATICAL MODEL

Consider the transient, two-dimensional, laminar, thermo-convection in an electrically-conducting Newtonian (liquid metals with $Pr=0.054$) fluid-saturated rectangular porous media enclosure with an upper free surface, enclosure height H and length L with internal heat generation present, in an (x,y) coordinate system, where x is parallel to the base of the enclosure and y is normal to it. A magnetic field, \mathbf{B}_0 , is applied parallel to the horizontal axis. The physical system is illustrated in **Figure 1**. In consistency with magnetohydrodynamics, following Cramer and Pai [53], the Maxwell equations define the electromagnetic body force exerted on the electrically conducting Newtonian fluid and the electrical current, \mathbf{J} take the form:

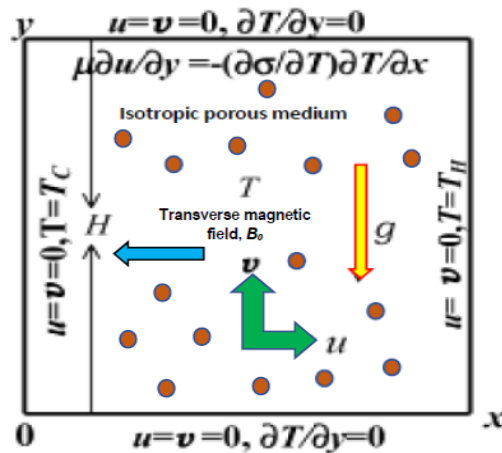


Fig 1: Physical model for hydromagnetic Marangoni semiconductor melt porous enclosure

Ohm's' Law

$$\mathbf{J} = \sigma(-\nabla\phi + \mathbf{V} \times \mathbf{B}) \quad (1)$$

Electrical Current Continuity:

$$\nabla \cdot \mathbf{J} = 0 \quad (2)$$

Lorentz Body Force Equation:

$$\mathbf{F} = \mathbf{J} \times \mathbf{B} \quad (3)$$

For the present case the boundaries of the enclosure are electrically-insulated and therefore the electrical potential, ϕ , in (1) is constant, so that following Gelfgat and Bar-Yoseph [8], Eqn. (1) is simplified and leads to the final modified form of (4), viz:

$$\mathbf{F} = \sigma(\mathbf{V} \times \mathbf{B}) \times \mathbf{B} \quad (4)$$

The left-hand side and right-hand side walls of the enclosure are prescribed uniform temperatures, T_C and T_H respectively. The porous medium is assumed to be maintained in local thermal equilibrium and no stratification is present. Following Bég *et al.* [49, 51] a Darcy porous drag model is employed to simulate the effects of the retarding porous medium on the flow field. This takes the following form for general three-dimensional flow via an isotropic, homogenous, non-stratified, porous medium with high velocity effects:

$$\nabla p = -(\mu/K) \mathbf{V} \quad (5)$$

where \mathbf{V} designates the velocity vector, p is the hydrodynamic pressure, μ is the dynamic viscosity, K is hydraulic conductivity (permeability) of the porous material, ρ is the density of the fluid. A two-dimensional version of this equation with velocity vector $\mathbf{V} = (u, v, 0)$ is

employed in the current study. For isotropic flows the permeability is the same in all directions and therefore a single value, K , is used in the model. A linear variation of *surface tension*, σ^* , with temperature is employed in our model, taking the form:

$$\sigma^* = \sigma^*_0 [1 - \gamma(T - T_0)] \quad (6)$$

where the temperature coefficient of the surface tension, γ , is defined by the thermal gradient of surface tension:

$$\gamma = \frac{1}{\sigma^*_0} \frac{\partial \sigma}{\partial T} \quad (7)$$

In (6), σ^*_0 is the reference surface tension, T is the fluid temperature in the enclosure and T_0 is the mean of the temperatures of the heated and cooled walls of the cavity ($= (T_H + T_C)/2$). It is also assumed that the influence of Joule electro-thermal heating is negligible and that the magnetic field applied is insufficient to generate magnetic induction effects. Following Gelfgat and Bar-Yoseph [8] the upper boundary is assumed to be perfectly horizontal and fluid above this surface possesses negligible viscous and thermal conductivity properties, so that no influence is exerted on the enclosure convection regime. With the upper and lower boundaries of the enclosure also insulated, both thermally and electrically, introducing the above equations into the general transport equations, the governing conservation equations for mass, momentum and heat in the enclosure can be defined as follows:

$$\frac{\partial u}{\partial x} + \frac{\partial v}{\partial y} = 0 \quad (8)$$

$$\rho \left[\frac{\partial u}{\partial t} + u \frac{\partial u}{\partial x} + v \frac{\partial u}{\partial y} \right] = -p_x + \mu \nabla^2 u - \frac{\mu}{K} u \quad (9)$$

$$\rho \left[\frac{\partial v}{\partial t} + u \frac{\partial v}{\partial x} + v \frac{\partial v}{\partial y} \right] = -p_y + \mu \nabla^2 v - \frac{\mu}{K} v - \sigma B_0^2(v) + \rho g \beta (T - T_c) \quad (10)$$

$$\frac{\partial T}{\partial t} + u \frac{\partial T}{\partial x} + v \frac{\partial T}{\partial y} = \alpha \nabla^2 T + \frac{q'''}{\rho C_p} \quad (11)$$

where ∇^2 denotes the Laplacian operator. Only a y -direction Lorentzian magnetic body force in Eqn. (10) is invoked, which is transverse to the x -direction of application of the magnetic field. The corresponding boundary conditions (spatial and temporal) are imposed as follows at the *left wall, base wall and right wall*, which are fixed boundaries:

$$\text{At } t = 0 : u = v = T = 0 \quad (12)$$

$$u = v = 0, T = T_H \text{ for } 0 \leq y \leq H \text{ at } x = L \text{ (right wall)} \quad (13)$$

$$u = v = 0, T = T_C \text{ for } 0 \leq y \leq H \text{ at } x = 0 \text{ (left wall)} \quad (14)$$

$$u = v = 0, \frac{\partial T}{\partial y} = 0 \text{ for } 0 \leq x \leq H \text{ at } y = 0 \text{ (base wall)} \quad (15)$$

At the free surface (upper boundary), dynamic boundary conditions are required. A balance is needed between the surface tension gradient and shear stress at the free surface essential for generating thermo-capillary (Marangoni) convection in the enclosure. These are defined as follows:

$$u = v = 0, \frac{\partial T}{\partial y} = 0, -\frac{\partial \sigma}{\partial T} \frac{\partial T}{\partial x} = \mu \frac{\partial u}{\partial y} \text{ for } 0 \leq x \leq H \text{ at } y = H \text{ (upper free surface)} \quad (16)$$

3. TRANSFORMATION OF MODEL

For the mathematical model in terms of primitive variables, defined by Eqns. (8) to (11) with boundary conditions (12) to (16), a numerical solution is still complex. We therefore implement a series of dimensionless parameters to transform the system into non-dimensional form, a procedure which invokes key control parameters and avoids the need for actual thermo-physical properties in the computations. This leads to the *vorticity stream function* formulation for the problem and greatly facilitates numerical simulations using the MAC finite difference method [52]. Defining:

$$\begin{aligned} X &= \frac{x}{H}, Y = \frac{y}{H}, U = \frac{\partial \psi}{\partial Y} = \frac{uH}{\nu}, V = -\frac{\partial \psi}{\partial X} = \frac{vH}{\nu}, \Omega = -\nabla^2 \psi, \\ \tau &= \frac{t\nu}{H^2}, \theta = \frac{T - T_0}{T_H - T_0}, A = \frac{L}{H}, Da = \frac{K}{H^2}, \\ Gr &= \frac{g\beta(T_H - T_C)H^3}{\nu^2}, Pr = \frac{\nu}{\alpha}, \Gamma = 2\frac{Ra_l}{Ra}, \\ Ra_l &= \frac{g\beta q''' H^5}{k\alpha\nu}, Ma = -\frac{\partial \sigma}{\partial T} \frac{(T_H - T_C)}{\mu\alpha}, Ha = \frac{B_0 H \sqrt{\sigma}}{\sqrt{\mu}} \end{aligned} \quad (17)$$

Introducing these transformations, the conservation equations with new dependent variables Ω, U, V, θ now become in vorticity formulation, with $\nabla^2 \psi = -\Omega$:

Momentum

$$\frac{\partial \Omega}{\partial \tau} + \frac{\partial(U\Omega)}{\partial X} + \frac{\partial(V\Omega)}{\partial Y} = \nabla^2 \Omega + \frac{Gr}{2} \frac{\partial \theta}{\partial X} - Ha^2 \left[\frac{\partial V}{\partial X} \right] - \frac{1}{Da} \left(\frac{\partial V}{\partial X} - \frac{\partial U}{\partial Y} \right) \quad (18)$$

Heat

$$\frac{\partial \theta}{\partial \tau} + \frac{\partial(U\theta)}{\partial X} + \frac{\partial(V\theta)}{\partial Y} = \frac{1}{Pr} \nabla^2 \theta + \frac{\Gamma}{Pr} \quad (19)$$

The two original momentum equations are therefore reduced to a single equation in which Darcian drag terms are featured. The transformed conditions prescribed at the four boundaries now become:

$$\text{At } \tau = 0: U = V = \psi = \theta = 0 \quad (20)$$

$$U = V = \psi = 0, \theta = 0 \text{ for } 0 \leq Y \leq 1 \text{ at } X = 0 \quad (21)$$

$$U = V = \psi = 0, \theta = 1 \text{ for } 0 \leq Y \leq 1 \text{ at } X = A \quad (22)$$

$$U = V = \psi = 0, \frac{\partial \theta}{\partial Y} = 0, \Omega = \frac{\partial U}{\partial Y} = -\frac{Ma}{2Pr} \frac{\partial \theta}{\partial X} \text{ for } 0 \leq X \leq 1 \text{ at } Y = 1 \quad (23)$$

Of particular interest, in *magnetic/semiconductor materials processing*, is the non-dimensional rate of heat transfer which in terms of the *local Nusselt number*, may be defined, for the right heated vertical wall, as follows:

$$Nu = \frac{1}{2} \frac{qH}{k(T_H - T_C)} = -\frac{1}{2} \left[\frac{\partial \theta}{\partial X} \right]_{X=A} \quad (24)$$

The corresponding average Nusselt number, designated by Nu_{av} , may be computed as follows:

$$Nu_{av} = -\frac{1}{2} \int_0^1 \left(\frac{\partial \theta}{\partial X} \right) dY \quad (25)$$

4. MAC NUMERICAL SOLUTION AND VALIDATION

We employ a finite difference solver to solve equations (18) and (19) with initial and boundary conditions (20) to (24). This finite difference method (FDM) is stable, convergent and employs a collocation grid. The velocity–vorticity gradient causes strong coupling in the continuity equation and the projection method is implemented for the momentum equation (18). An in-house computational MATLAB-based version of this FDM code is employed in the simulations. The stream function is obtained by:

$$\nabla^2 \psi = -\Omega \quad (26)$$

This is solved by the well-known iterative Gauss Seidel method. The finite volume scheme is used for the advection terms and a second order central difference scheme is used for diffusion term. In the MAC approach although we consider viscous flow, viscosity is not actually required for numerical stability. The marker particles do not participate in the calculation. Based on the weak conservative form of the two-dimensional momentum and heat conservation equation a grid meshing procedure is deployed.

The convergence of the solution is assumed when the relative error for each of the variables satisfies the following convergence criteria:

$$\left| \frac{\lambda^{k+1} - \lambda^k}{\lambda^{k+1}} \right| \leq \chi$$

where k represents the iteration number and χ is the convergence criterion. In this study, the convergence criterion was set at $\chi = 10^{-6}$.

We adopt a uniform mesh size 80 X 80 in the present computations which successfully achieves mesh-independent results. Denser grids are not required as the modification in solutions is not significant beyond 80 X 80 dense grids. Validations with earlier studies conducted by de Vahl Davis [54], Manzari [55] and Wan *et al.* [56] are also included and summarized in **Tables 1 and 2**. These validations are conducted for $Pr = 0.71$ (air), $Ha = Ma = \Gamma = 0$ and $Da \rightarrow \infty$. Excellent agreement is obtained with the 80X80 grid design. Confidence in the FDM solver is therefore justifiably high. The present MATLAB-based MAC code has also been used recently in a variety of enclosure convection flows including free convection in a trapezoidal enclosure [57] and radiative convection in a trapezoidal enclosure [58]. The grid differencing scheme is shown in **Fig. 2**. The mesh designs for three different aspect ratio enclosures are given in **Figs. 3a-c**.

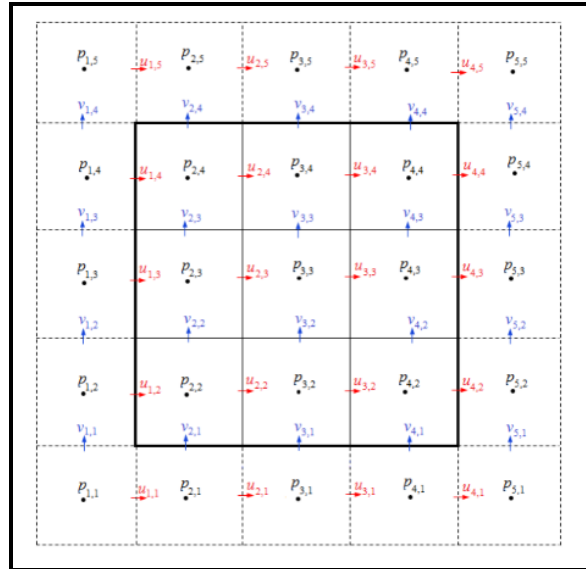
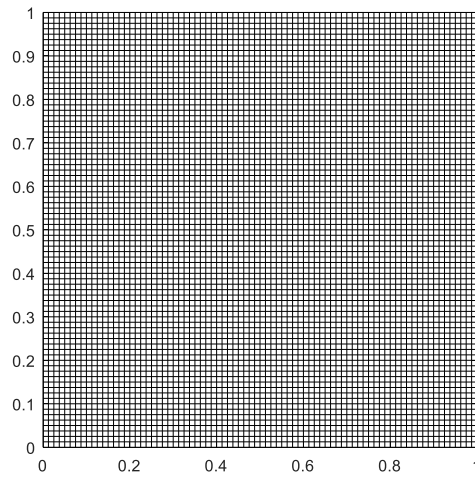


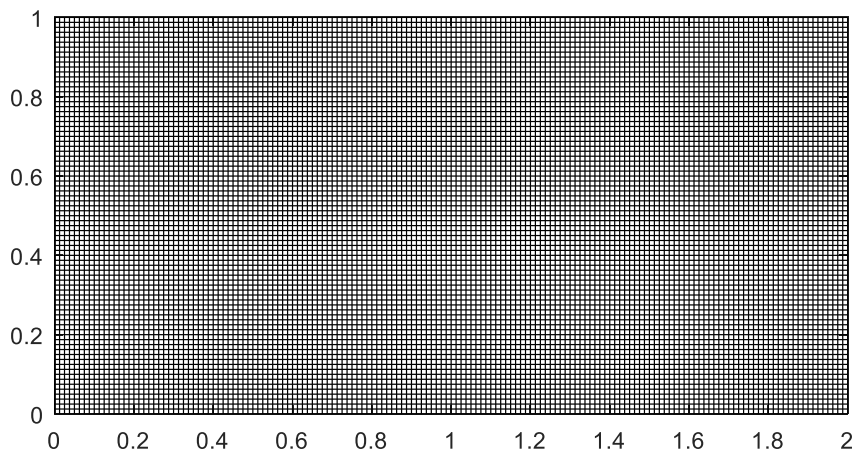
Fig. 2 MAC grid finite differencing procedure

Table. 1. Grid independence and validation for Average Nusselt number (Nu) with $Pr = 0.71$

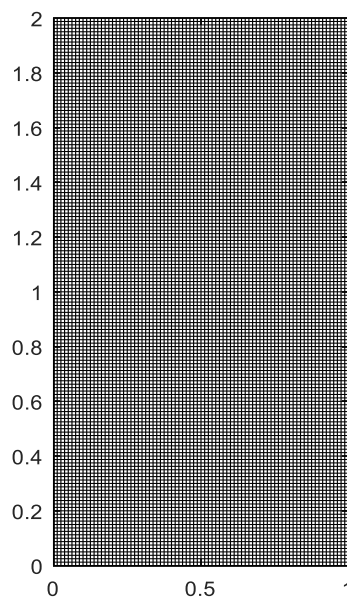
Ra	Nu	Ref. [54]	Ref. [55]	Ref. [56] FEM	Present study 40X40	Present study 80X80	Present study 120X120	Present study 160X160
10^4	Average	2.243	2.084	2.254	2.2526	2.2455	2.2444	2.2442



a



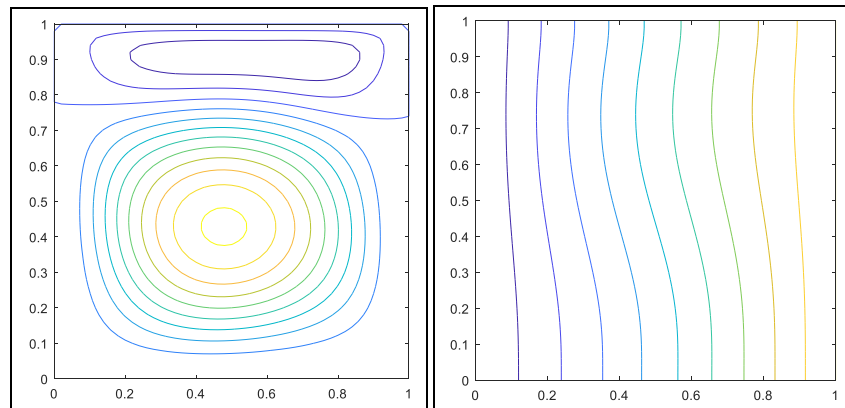
b



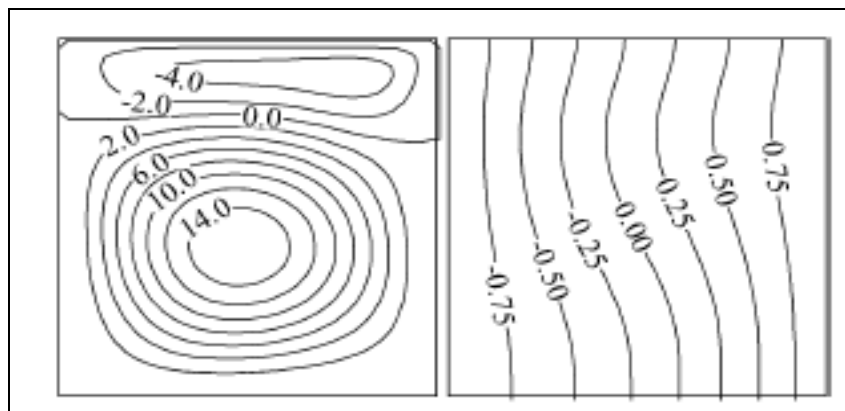
c

Figure 3a-c: Uniform mesh collocate grid for FDM with different aspect ratios a) $A=1$ (square), b) $A=0.5$ (shallow), c) $A=2$ (tall)

In addition to the mesh-independence and previous validations for average Nusselt number, further corroboration of the FDM simulations is conducted against the ADI solutions of Hossain *et al.* [48] and these are visualized in **Figs. 4-5** for both non-magnetic ($Ha = 0$) and strong magnetic cases ($Ha = 20$).



(a)



(b)

Fig 4: a)Streamlines and b) isotherms for $Gr = 2 \times 10^4$ and $Pr = 0.054$ and $Ma = 100$ while $Ha = 0$ (absent magnetic field) and $\lambda = 0$ for $Da \rightarrow \infty$ (no porous media effects) (top colour plots-MAC solution, below Hossain *et al.* [48])

Excellent correlation is achieved for both streamline and isotherm distributions. The dual vortex structure with asymmetry is captured in the streamline plot and smooth disparate isotherms are computed also in **Fig. 4** when magnetic field is absent ($Ha = 0$). These plots correspond to an aspect ratio of 1 and semiconductor melt ($Pr = 0.054$ for which thermal diffusivity greatly exceeds the momentum diffusivity and thermal conductivity is extremely high). **Fig. 5a** shows that with strong horizontal magnetic field ($Ha = 20$), and thermal buoyancy a hundred times stronger and Marangoni effect ten times stronger ($Gr = 2 \times 10^6$ and $Ma = 1000$ in **fig. 5a** compared with $Gr = 2 \times 10^4$ and $Ma = 100$ in **Fig. 4**) the original upper laterally dispersed vortex structure is constricted into the top left corner owing to damping of the flow and the lower vortex expands. The isotherms are warped significantly

and evolve into sigmoidal distributions with more intense clustering near the upper left wall and the lower right wall, exactly as computed in [48], although the black and white plots in [48] are considerably less clear. **Fig. 5b** shows that the comparison of present study and experimental study [64], the comparison gives the confidence for the numerical method. The experimental study of semiconductors melts is addressed by GAMM Workshop [62]. Confidence in the MAC simulations is therefore very high.

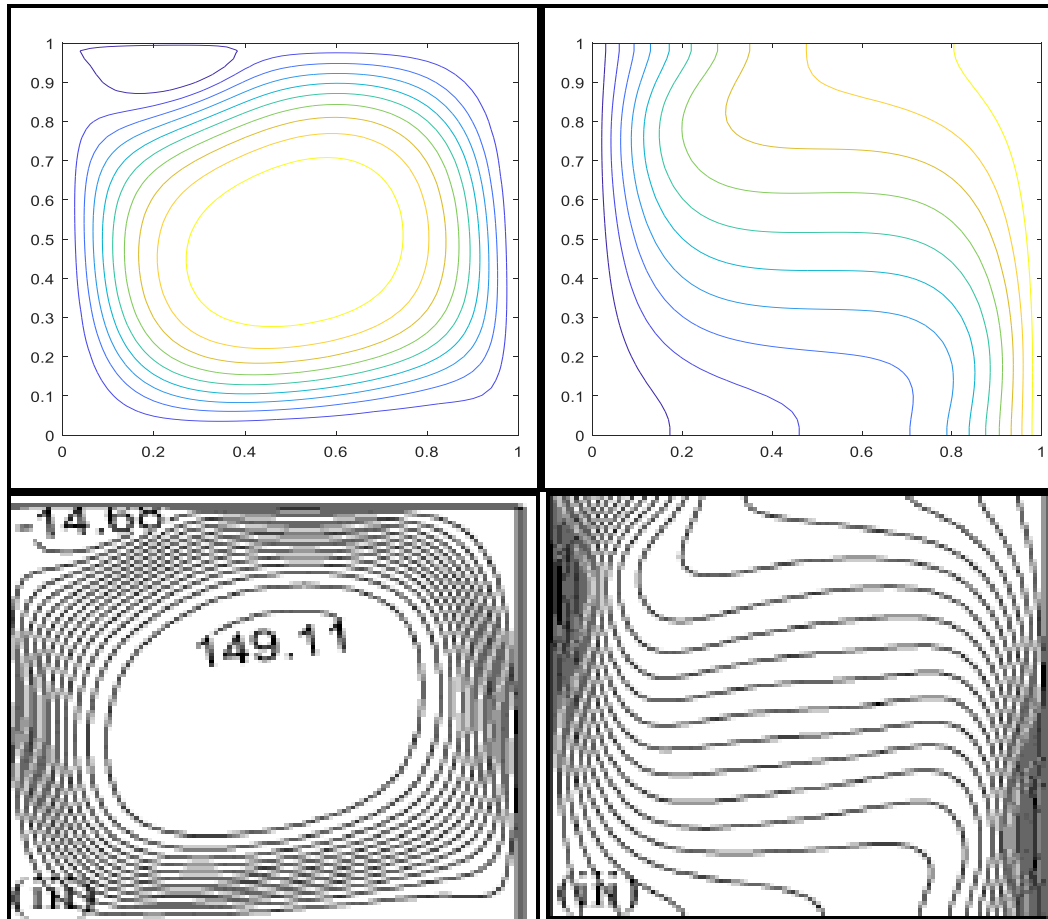


Fig 5a: a) Streamlines and b) isotherms for $Gr = 2 \times 10^6$, and $Pr = 0.054$ and $Ma = 1000$ while $Ha = 20$ (strong horizontal magnetic field) and $\lambda = 0$ for $Da \rightarrow \infty$ (no porous media effects) (top colour plots-MAC solution, below Hossain *et al.* [48])

Table. 2. Comparison of Average Nusselt number (Nu) with $Pr = 0.71$

Ra	Nu	Ref. [54]	Ref. [55]	Ref. [56]	Present study
				FEM	(MAC)
10^3	Average	1.12	1.074	1.117	1.1185
10^4	Average	2.243	2.084	2.254	2.2526
10^5	Average	4.52	4.3	4.598	4.5907
10^6	Average	8.8	8.743	8.976	8.9905

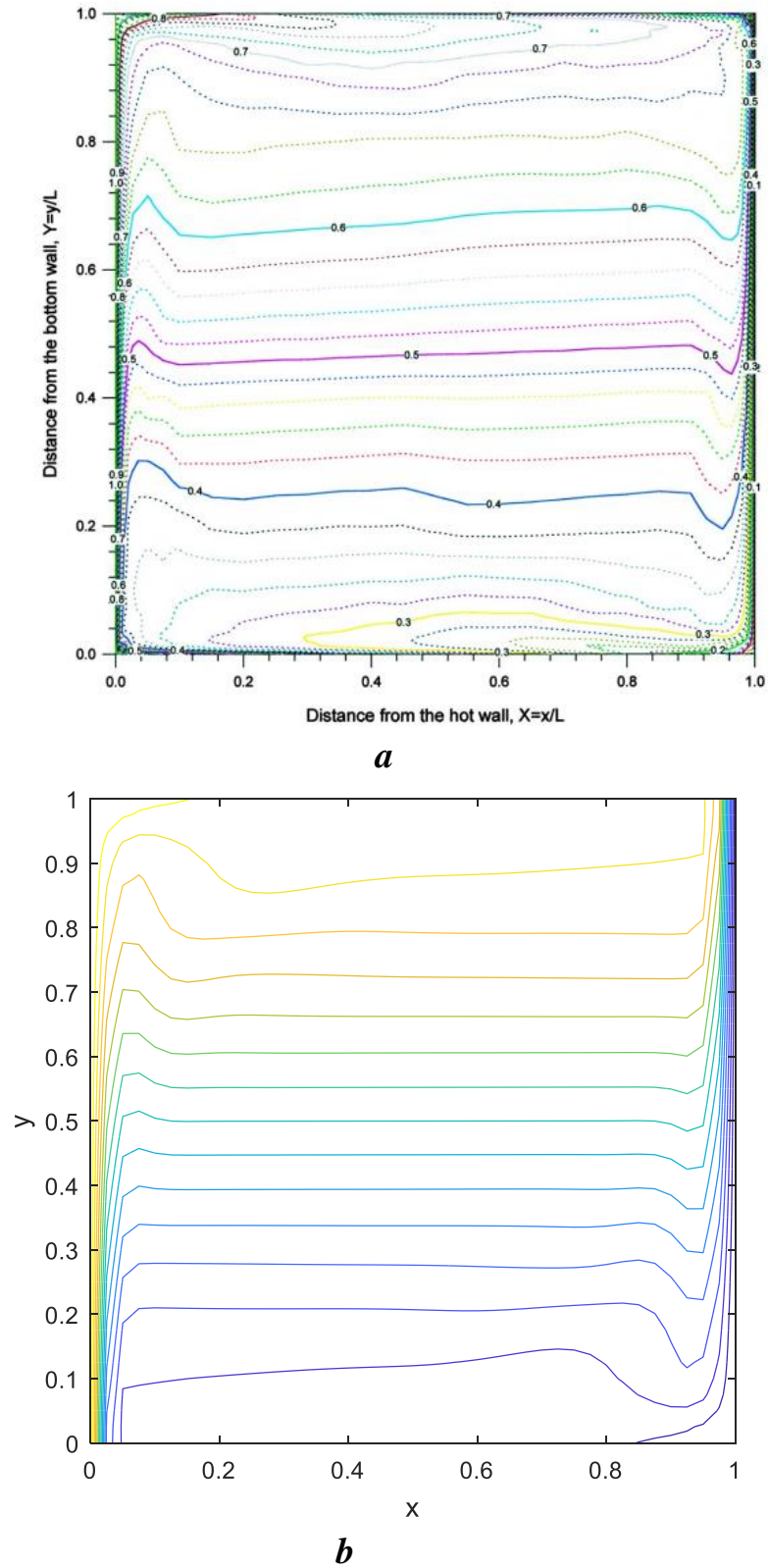


Fig 5b: Contour plot of temperature distribution, natural convection in an air filled cavity for a Rayleigh number of 1.58×10^9 . An experimental study [64] –a, Present study –b.

5. MAC NUMERICAL RESULTS FOR GENERAL MODEL

The general mathematical model defined by the Eqns. (18), (19) with boundary conditions (20)-(23) features 6 parameters. These are: *surface tension (thermocapillary) effect number* i.e. *Marangoni number* (Ma), *Prandtl number* (Pr), *Grashof number for buoyancy effects* (Gr), *Hartmann hydromagnetic number* (Ha), *Darcy number for bulk porous resistance* (Da), *Internal heat generation parameter* (I) and additionally an *aspect ratio* (A) can be varied. All MAC solutions are visualized for these parameters in **Figs. 6-22**. **Figs. 6(a-d)-8(a-d)** show the MAC results for variation in Darcy number (Da) and 3 different aspect ratios ($A = 0.5, 1, 2$).

Inspection of **Figs. 6a-d** reveals a significant evolution in isotherms and a weaker modification in streamline distributions with greater Darcy number. At very low Darcy numbers ($Da = 0.0001$), the permeability in the regime is extremely low. This generates significant Darcian resistance to the Marangoni magnetic convection and asymmetric single vortex structure is computed for streamlines. The isotherms are also largely undistorted with a slight warping towards the right-hand side as they approach the base wall of the enclosure. As Darcy number increases to $Da = 0.001, 0.01$ to 0.1 , streamlines morph leading to an asymmetric distribution and the vortex structure is larger towards the left cold wall boundary and constricts somewhat towards the right cooler wall. However, a single trapped cell is still sustained. A more significant modification is computed in the isotherms which are progressively constricted in the vicinity of the left wall and expand in the central zone, with considerably more divergence towards the lower base wall. This is also accompanied by a clustering of isotherms towards the right wall. Evidently the increase in Darcy number corresponds to a greater permeability which permits increased circulation of the hot fluid in the enclosure. These plots correspond to the “shallow” enclosure case ($A = 0.5$). the influence of Darcy number concurs with earlier studies in the field including Alchaar *et al.* [16] and also Alsabery *et al.* [17] who have also reported significant warping of isotherms with greater Darcy numbers in porous media magnetohydrodynamic convection, although in the absence of Marangoni surface tensions effects. **Figs. 7a-d** which correspond to a square enclosure ($A = 1$) and show the evolution of streamlines and isotherms over the same increment in Darcy number, are similarly found to exhibit a warping in the single cell vortex structure. However, the modifications are more towards the upper left corner and lower right corner of the enclosure, rather than towards the left wall alone. Isotherms are also less clustered towards the left and right walls with increasing Darcy number and a more even isotherm distribution (which remains warped towards the top left corner and lower base wall) is achieved, as compared with **Figs. 6a-d**.

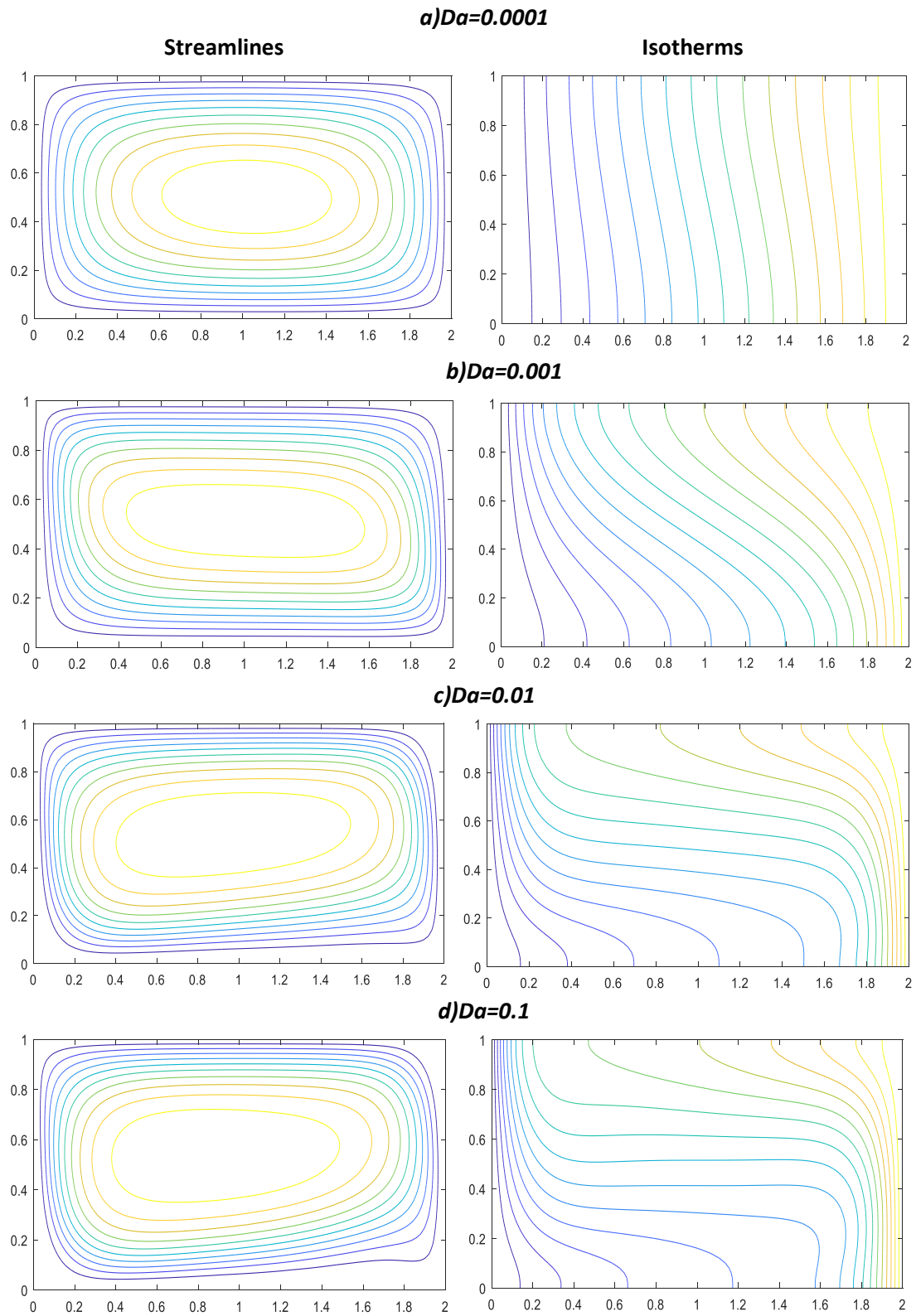


Fig. 6(a-d): Streamline and isotherm plots with $Gr=2 \times 10^5$, $Ha = 5.0$, $Pr=0.054$, $Ma=100$, $\Gamma=0$ (absent heat generation) for $A=0.5$ (shallow enclosure) for various Darcy numbers (Da)

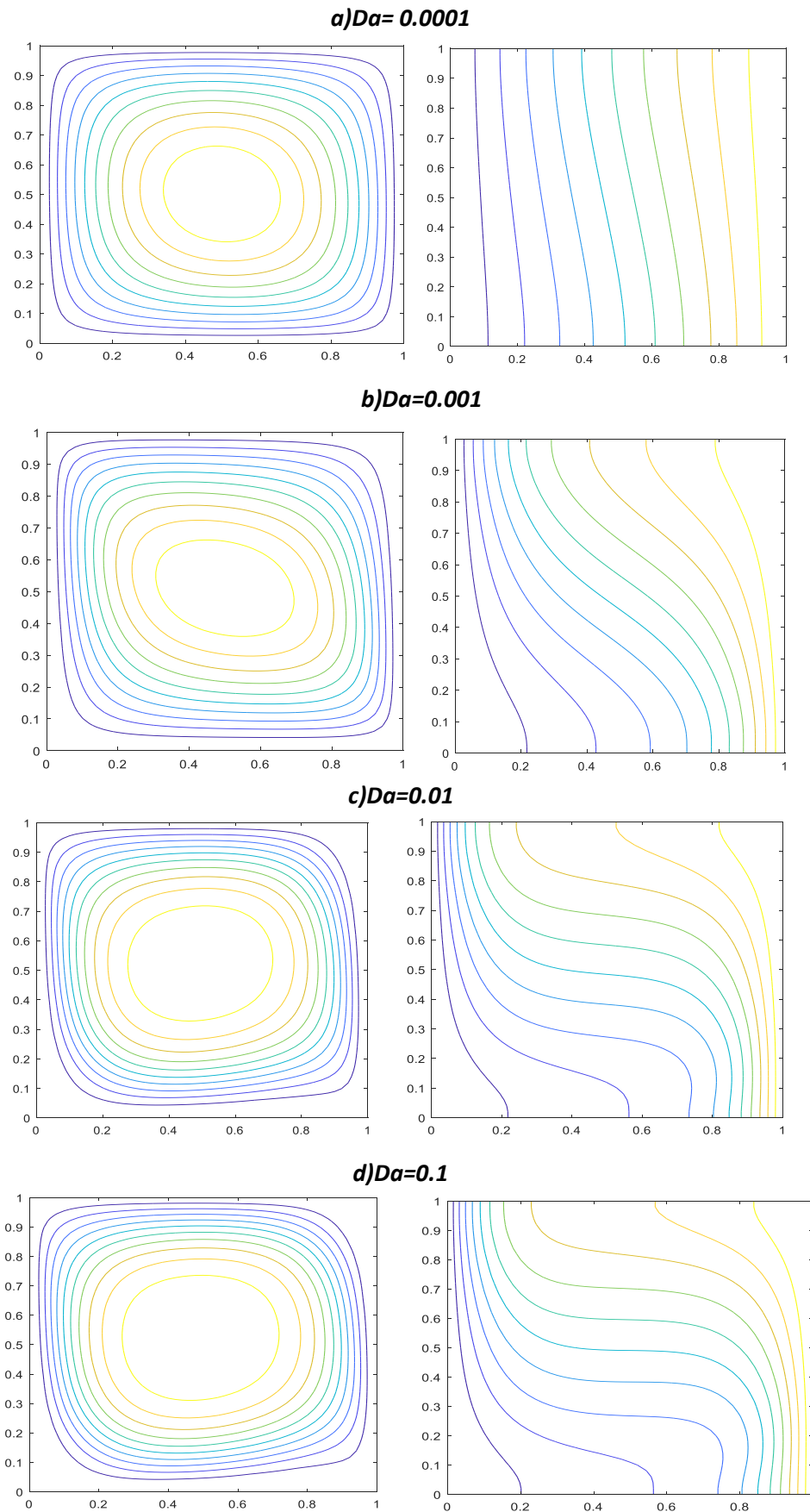
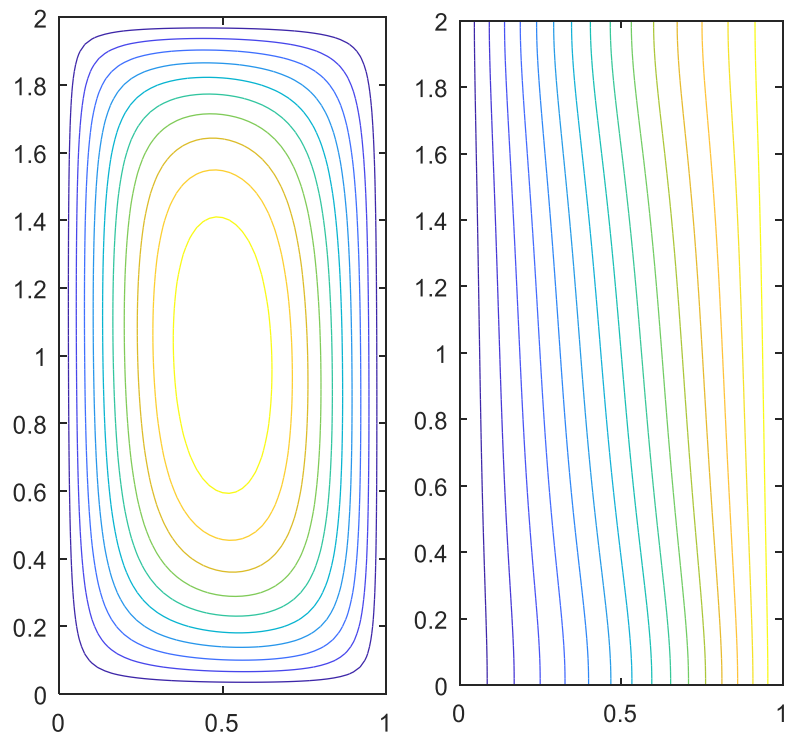
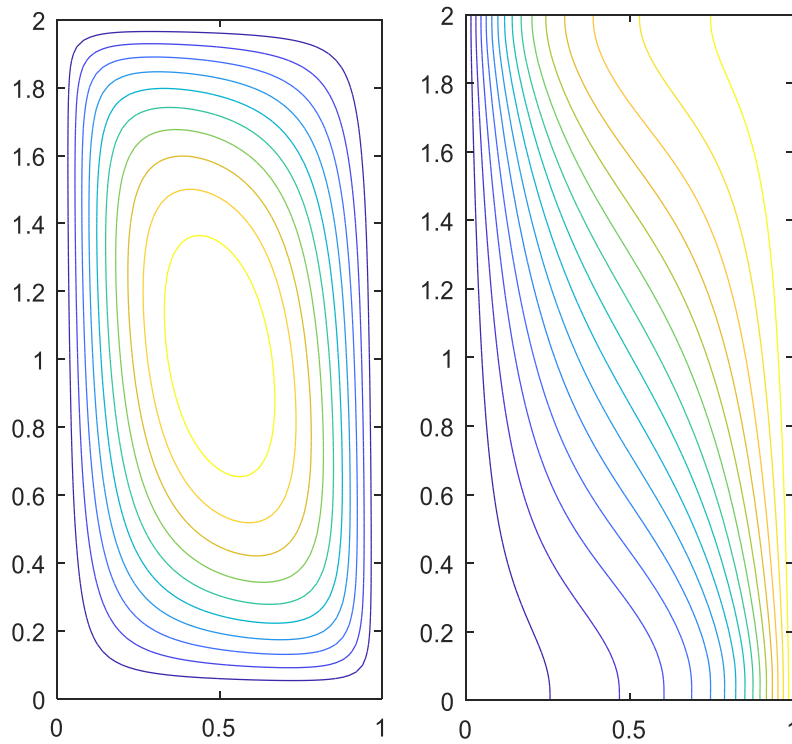


Fig. 7(a-d): Streamline and isotherm plots with $Gr=2 \times 10^6$, $Ha = 5.0$, $Pr=0.054$, $Ma=100$, $\Gamma=0$ (absent heat generation) for $A=1.0$ (square enclosure) for various Darcy numbers (Da)

a) $Da=0.0001$ **b) $Da=0.001$** 

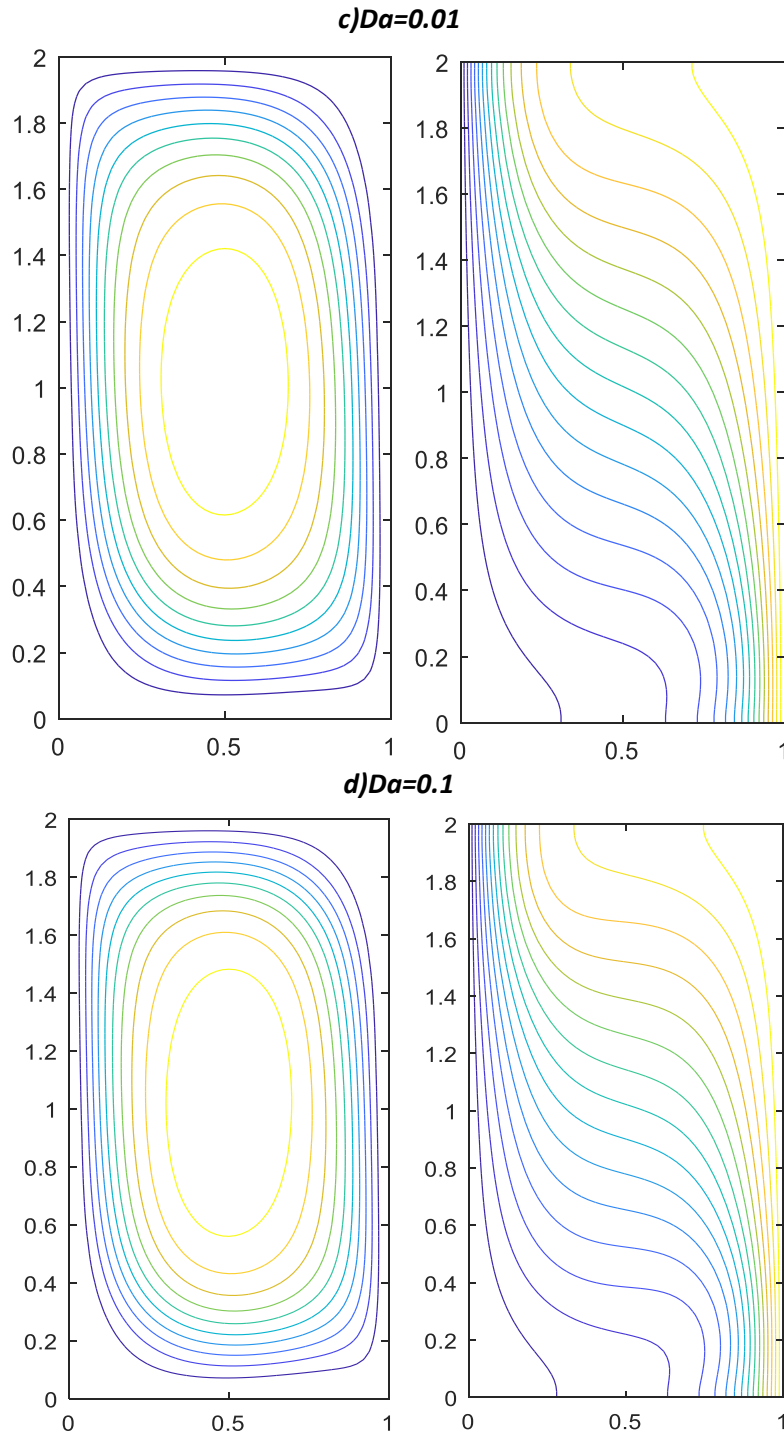


Fig. 8(a-d): Streamline and isotherm plots with $Gr=2 \times 10^6$, $Ha = 5.0$, $Pr=0.054$, $Ma=100$, $\Gamma=0$ (absent heat generation) for $A=2.0$ (tall enclosure) for various Darcy numbers (Da)
Figs. 8a-d indicate that again over an increment in Darcy number (Da) there is a distortion in isovels (streamlines) in the tall enclosure, towards the upper left corner and lower right corner of the enclosure, although significant stretching in the vertical direction is induced. Isotherms are also observed to become increasingly sigmoidal in nature and orientated more towards the top left and base wall than for the square enclosure, but less so than for the shallow enclosure.

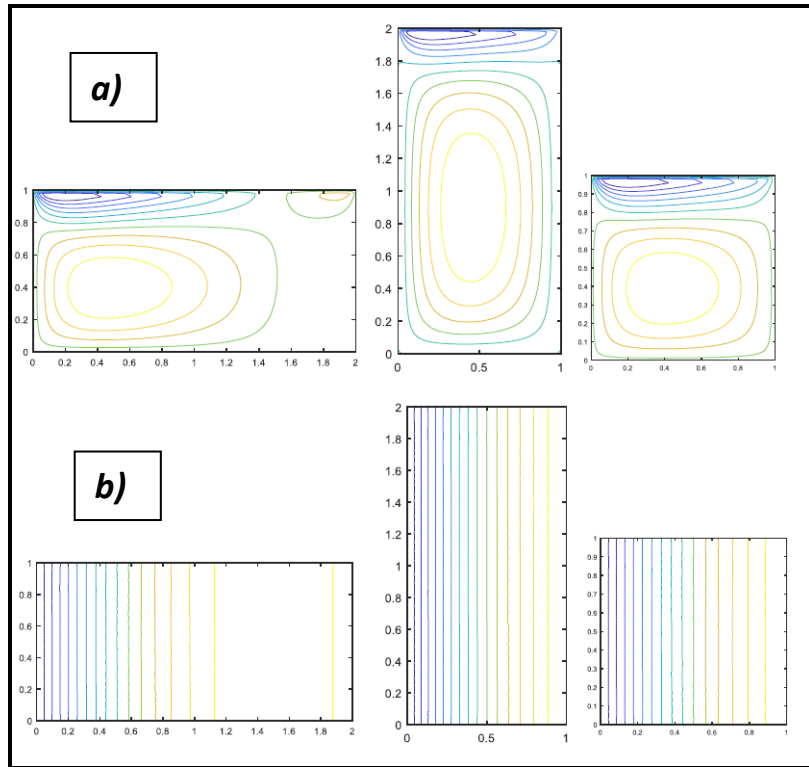


Fig. 9: a) Streamline and b) isotherm plots with $Gr=2 \times 10^4$, $Ha = 20$, $Pr=0.054$, $Ma=100$, $Da = 0.0001$ with $\Gamma=1$ for 3 different aspect ratios ($A=0.5, 2, 1$)

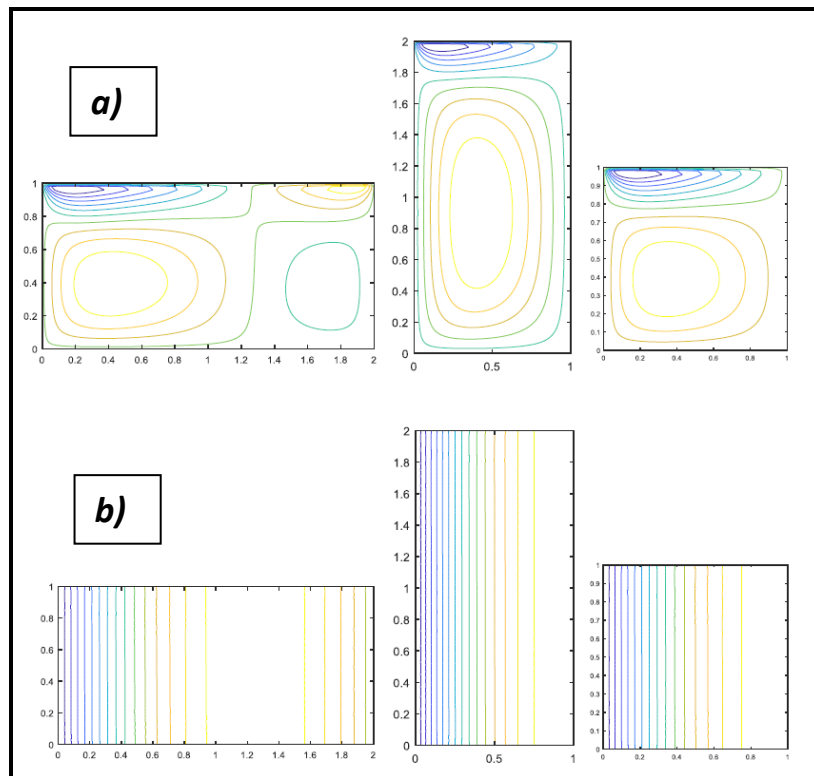


Fig. 10: a) Streamline and b) isotherm plots with $Gr=2 \times 10^4$, $Ha = 20$, $Pr=0.054$, $Ma=100$, $Da = 0.0001$ with $\Gamma=2$ for 3 different aspect ratios ($A=0.5, 2, 1$)

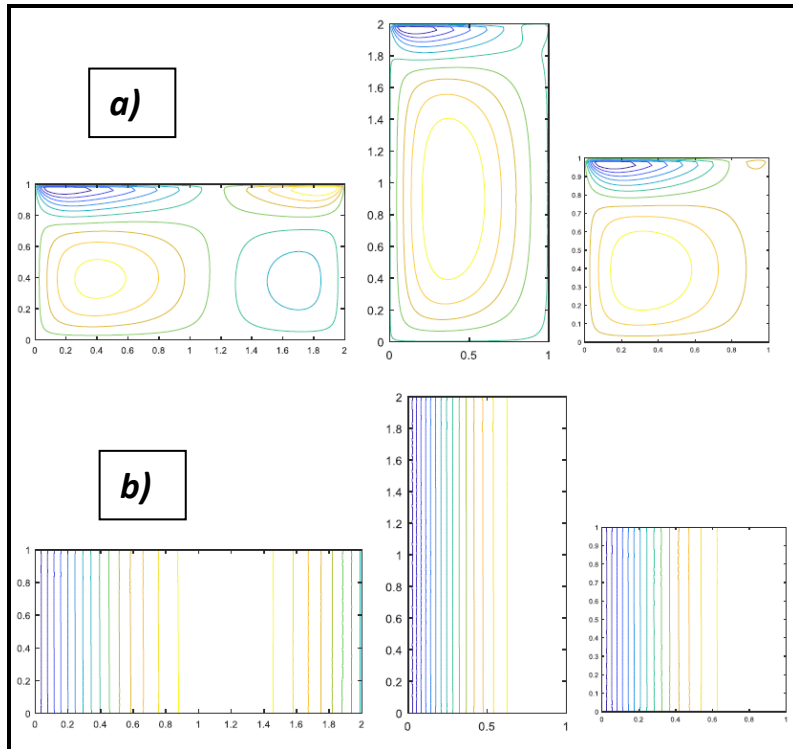


Fig. 11 a) Streamline and b) isotherm plots with $Gr=2 \times 10^4$, $Ha = 20$, $Pr=0.054$, $Ma=100$, $Da = 0.0001$ with $\Gamma=3$ for 3 different aspect ratios ($A=0.5, 2, 1$)

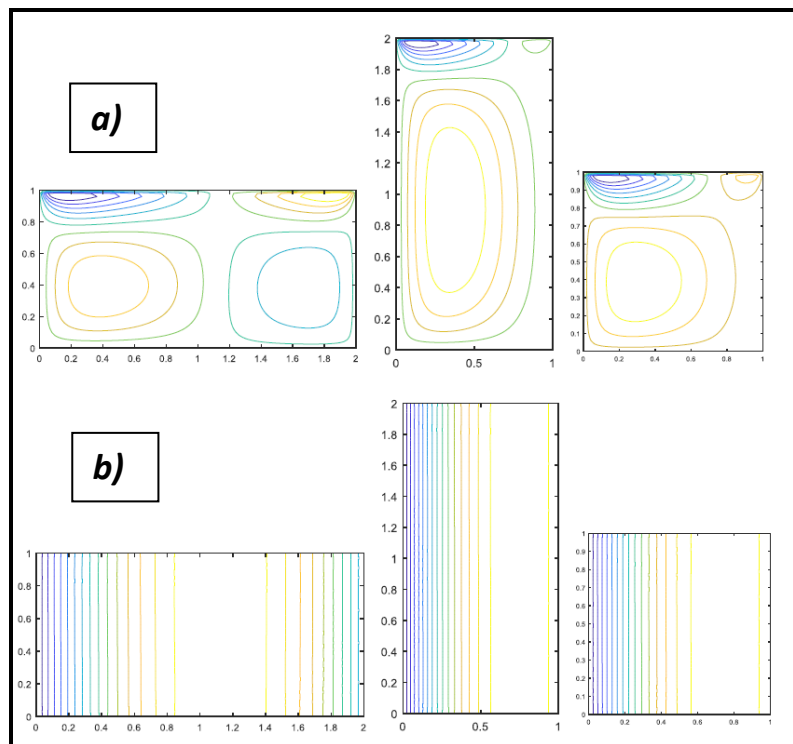


Fig. 12 a) Streamline and b) isotherm plots with $Gr=2 \times 10^4$, $Ha = 20$, $Pr=0.054$, $Ma=100$, $Da = 0.0001$ with $\Gamma=4$ for 3 different aspect ratios ($A=0.5, 2, 1$)

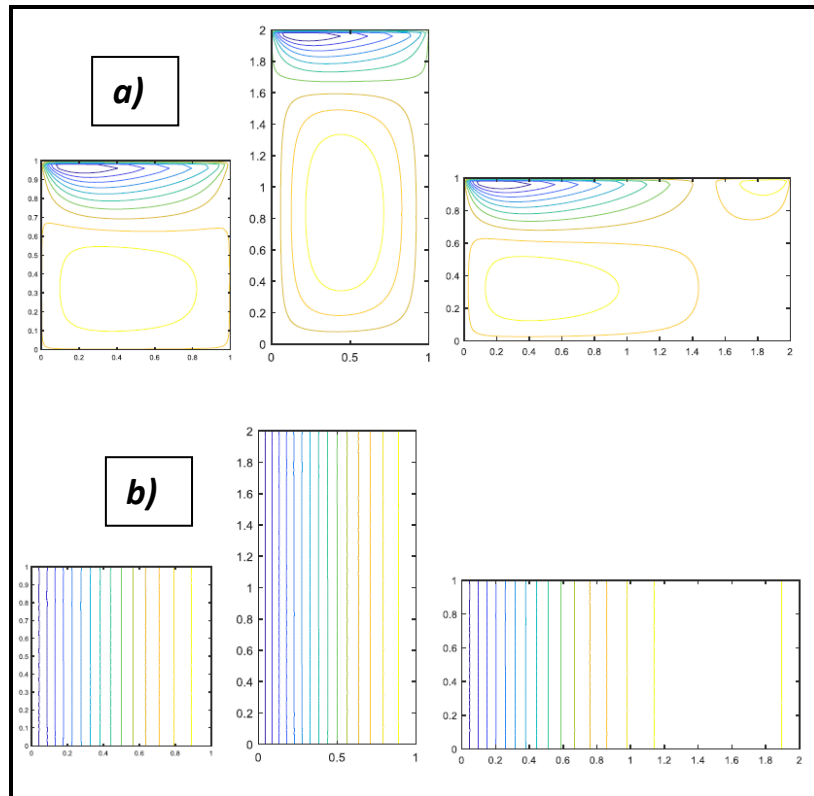


Fig. 13 a) Streamline and b) isotherm plots with $Gr=10^4$, $Ha = 20$, $Pr=0.054$, $Ma=100$, $Da=0.0001$ with $\Gamma=1$ for 3 different aspect ratios ($A=0.5, 2, 1$)

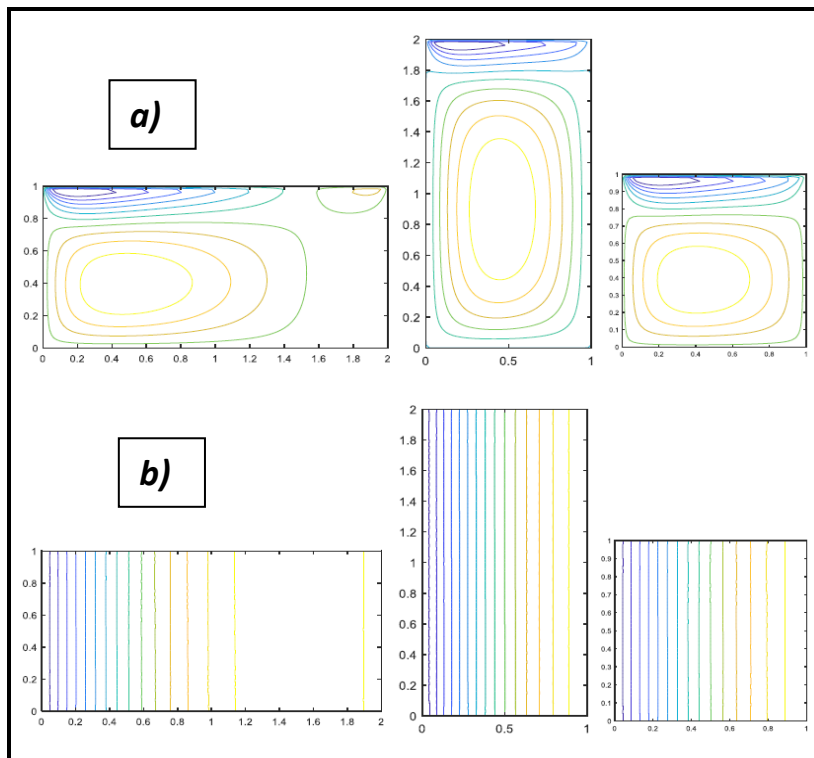


Fig. 14 a) Streamline and b) isotherm plots with $Gr= 2 \times 10^4$, $Ha = 20$, $Pr=0.054$, $Ma=100$, $Da=0.0001$ with $\Gamma=1$ for 3 different aspect ratios ($A=0.5, 2, 1$)

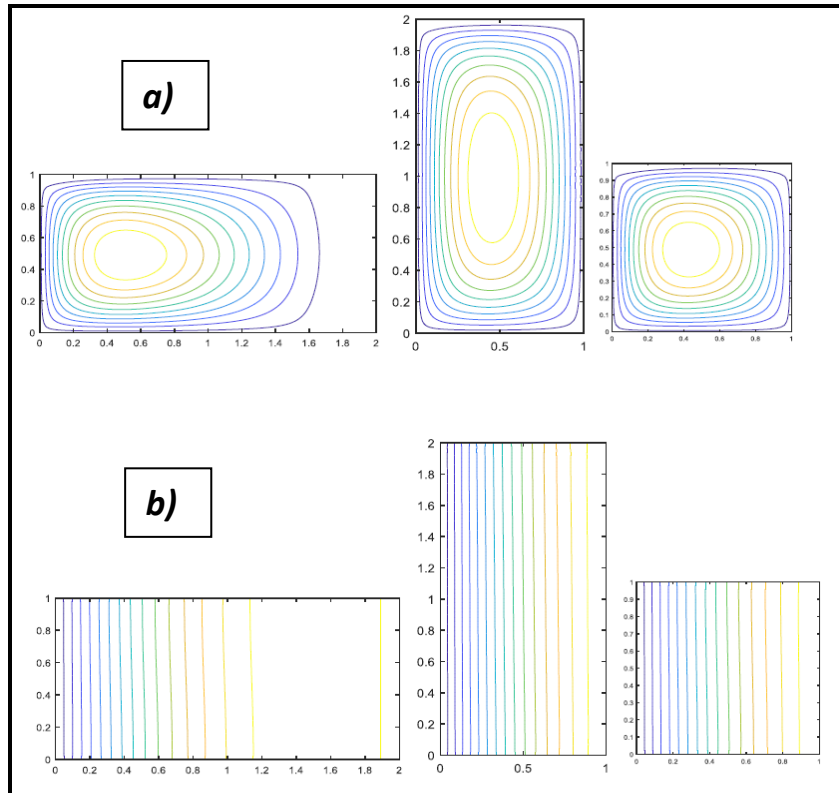


Fig. 15 a) Streamline and b) isotherm plots with $Gr = 2 \times 10^5$, $Ha = 20$, $Pr = 0.054$, $Ma = 100$, $Da = 0.0001$ with $\Gamma = 1$ for 3 different aspect ratios ($A = 0.5, 2, 1$)

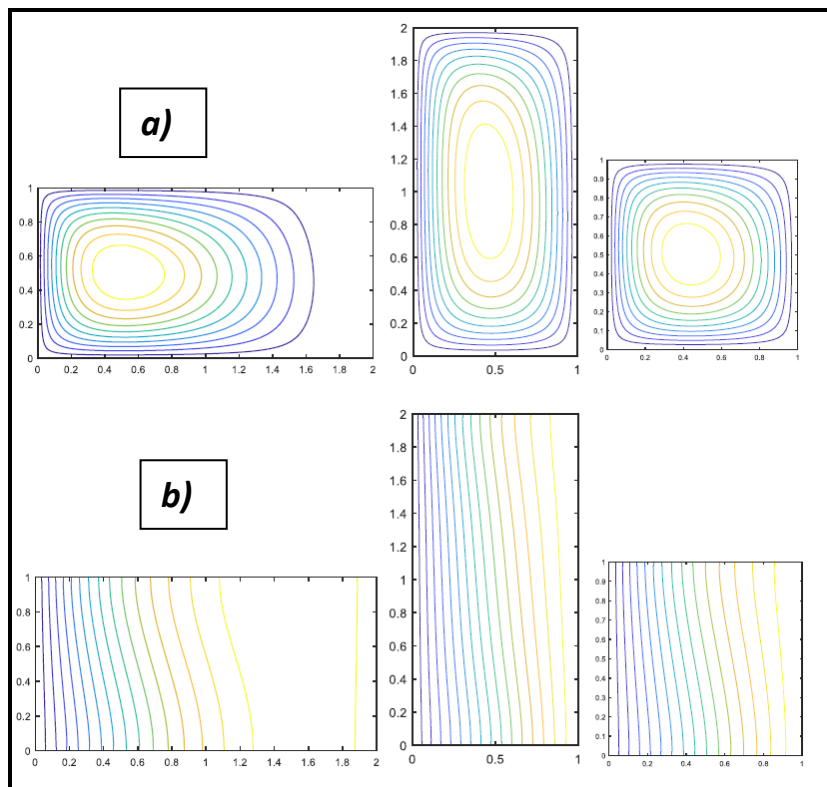


Fig. 16 a) Streamline and b) isotherm plots with $Gr = 2 \times 10^6$, $Ha = 20$, $Pr = 0.054$, $Ma = 100$, $Da = 0.0001$ with $\Gamma = 1$ for 3 different aspect ratios ($A = 0.5, 2, 1$)

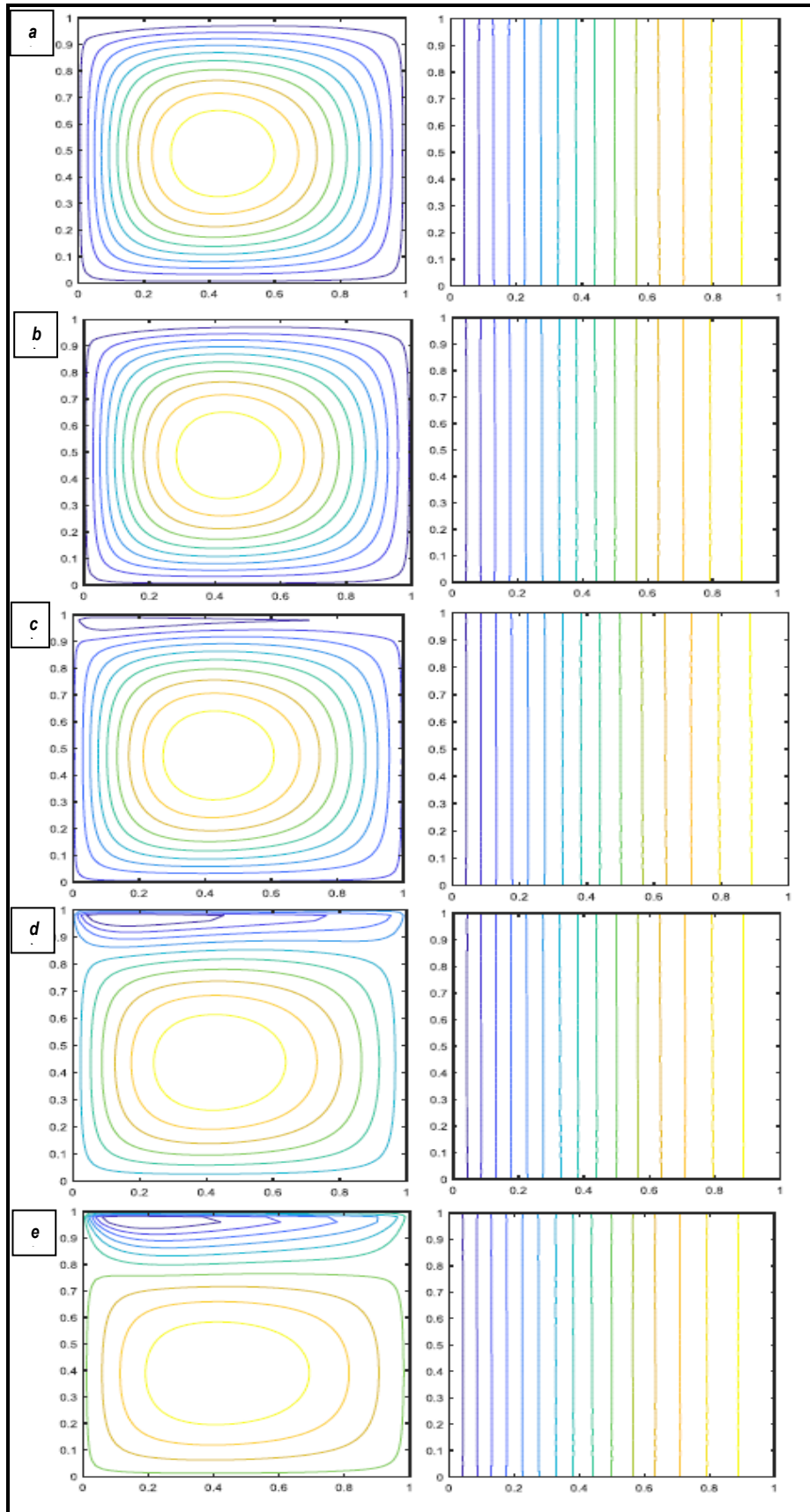


Fig. 17 (a-e) left - Streamline and right- isotherm plots with $Gr= 2 \times 10^4$, $Ha = 20$, $Pr=0.054$, $Da = 0.0001$ with $\Gamma=1$ for square enclosure ($A = 1$) with $Ma = a)1, b)10, c)20, d)50, e) 100$.

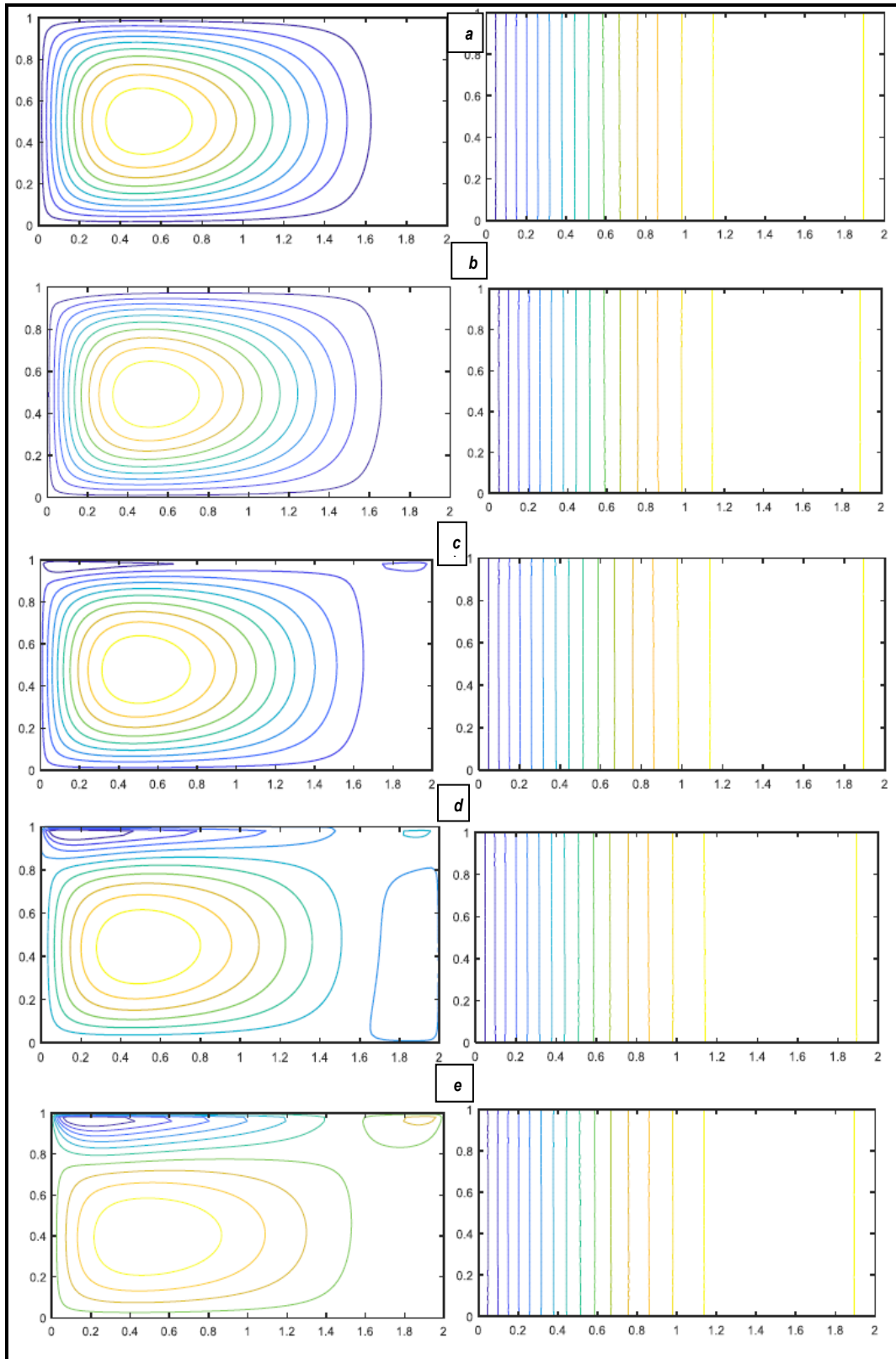


Fig. 18 (a-e) left - Streamline and right- isotherm plots with $Gr= 2 \times 10^4$, $Ha = 20$, $Pr=0.054$, $Da = 0.0001$ with $\Gamma=1$ for shallow enclosure ($A = 0.5$) with $Ma = a)1, b)10, c)20, d)50, e) 100$.

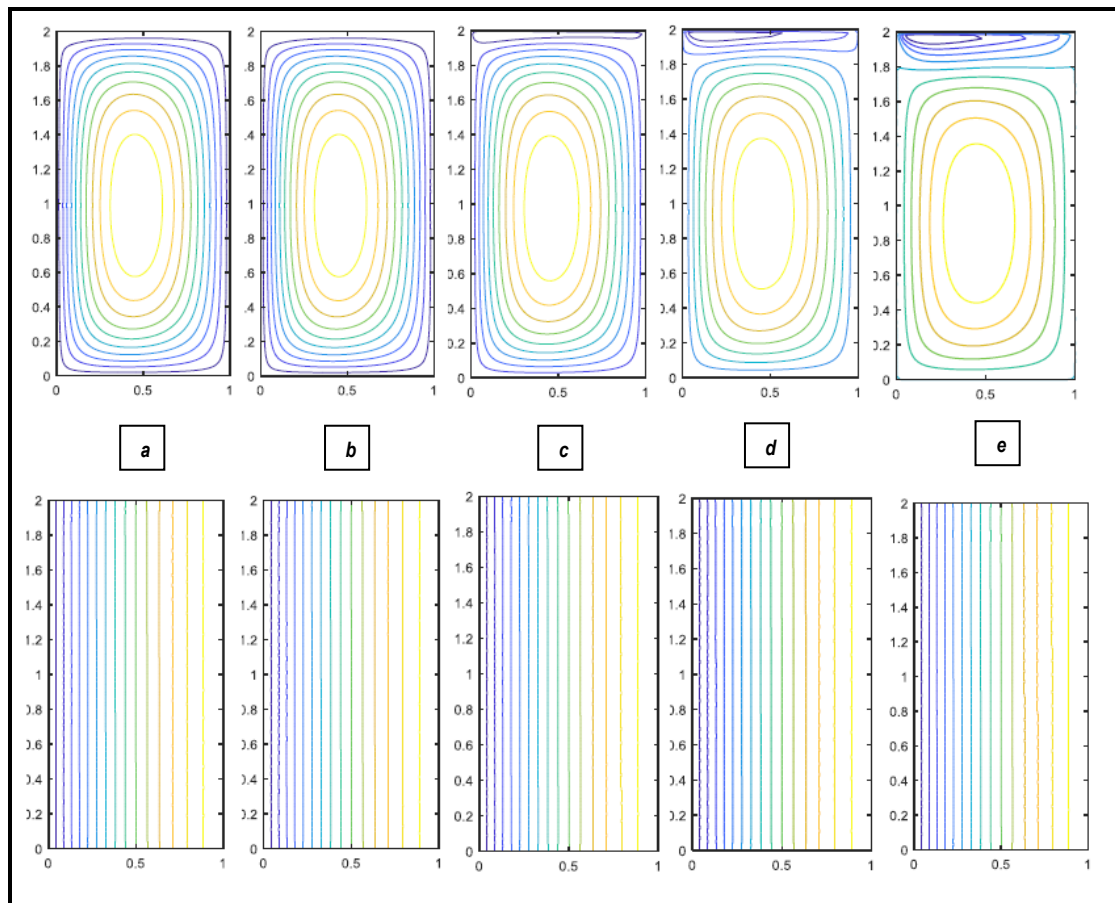


Fig. 19 (a-e) top - Streamline and **bottom** - isotherm plots with $Gr = 2 \times 10^4$, $Ha = 20$, $Pr = 0.054$, $Da = 0.0001$, $\Gamma = 1$ for tall enclosure ($A = 2$) with $Ma = a) 1, b) 10, c) 20, d) 50, e) 100$.

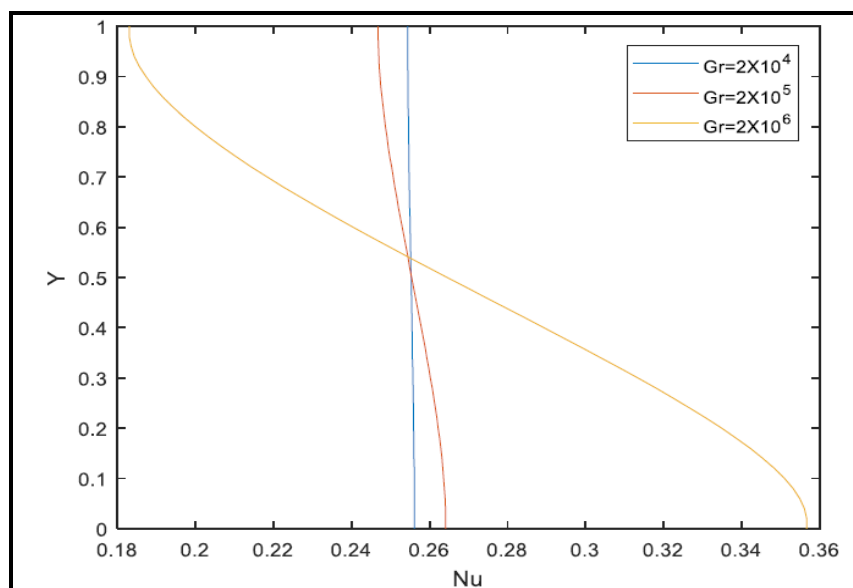


Fig. 20 – Local Nusselt number at hot right wall with $Ha = 5$, $Pr = 0.054$, $Ma = 10$, $Da = 0.0001$ and $\Gamma = 1$ for square enclosure ($A = 1$) with various Grashof numbers (Gr).

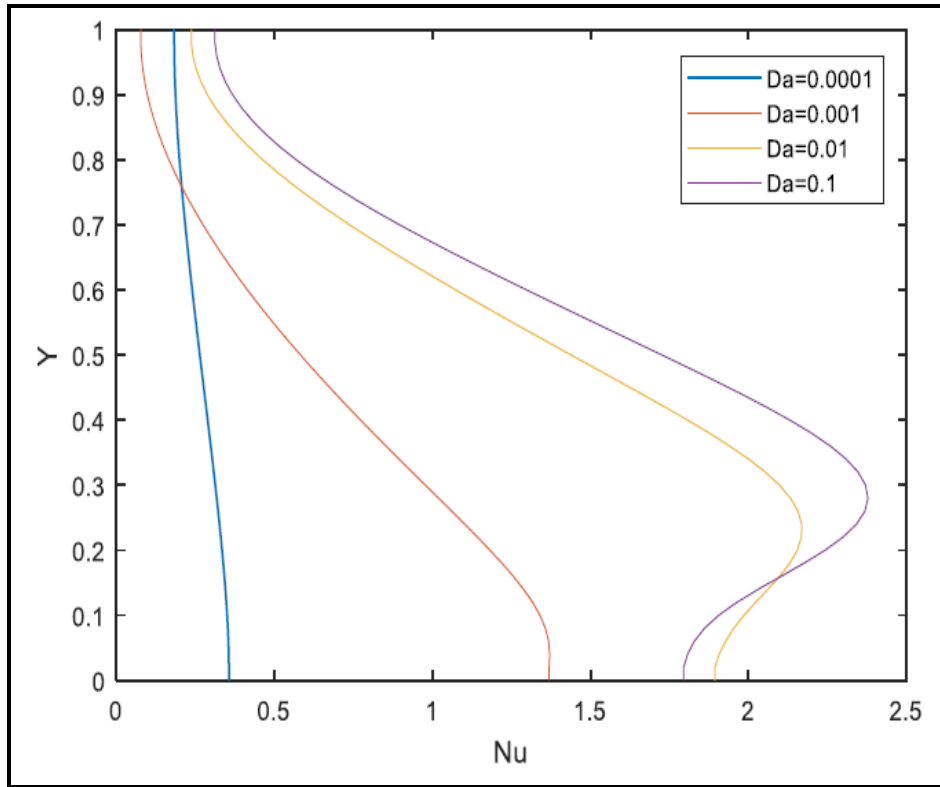


Fig. 21 – Local Nusselt number at hot right wall with $Ha = 5$, $Pr=0.054$, $Gr = 2 \times 10^6$, $Ma = 100$, $\Gamma=1$ for square enclosure ($A = 1$) with various Darcy numbers (Da).

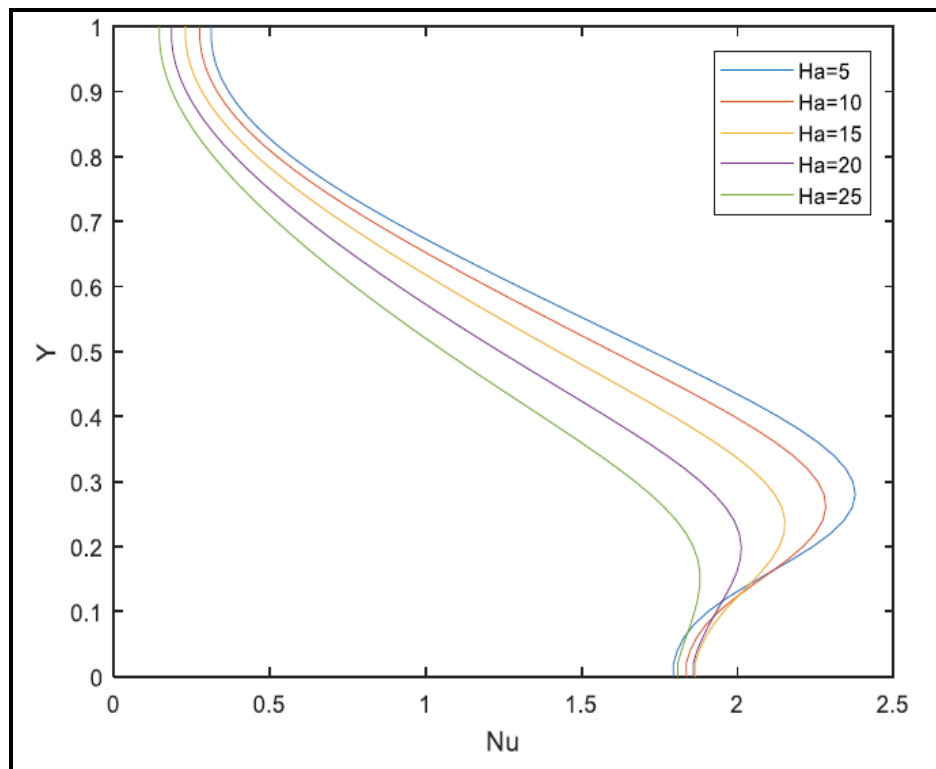


Fig. 22 – Local Nusselt number at hot right wall with $Pr=0.054$, $Gr = 2 \times 10^6$, $Ma = 100$, $Da = 0.1$, $\Gamma=1$ for square enclosure ($A = 1$) with various Hartmann numbers (Ha).

Fig. 9: a- b to 12a-b visualize the influence of increasing heat generation (source) parameter, Γ , on streamline for 3 different enclosure aspect ratios ($A=0.5, 2, 1$). Here significant but not excessive thermal buoyancy is imposed ($Gr=2\times 10^4$), strong transverse magnetic field ($Ha = 20$) for semiconductor melt ($Pr=0.054$) with weak thermocapillary convection ($Ma=100$) and minimum permeability ($Da = 0.0001$) i.e. a tightly packed porous medium. Evolution in the velocity and temperature fields can therefore be understood by comparing respective figures in these plots. **Figs. 9 a- b** imply that for $\Gamma=1$, a *triple vortex structure* is present with $A = 0.5$ (shallow enclosure) whereas dual cells are present in the enclosures for $A = 2$ and $A=1$. In the latter cases (i.e. tall and square enclosures) an approximately symmetrical larger cell occupies the majority of the lower half space with a smaller partial cell emerging in the upper half space, which tends to grow from the left upper corner and disperses laterally in the horizontal direction. However, for the shallow enclosure, the lower dominant cell is biased towards the left colder wall with an absence of any cell in the lower right corner. A second smaller cell grows from the upper left corner along the top boundary but does not extend to the right corner and terminates before this. A third cell is observed in the upper right corner which is much smaller than the primary and secondary vortex structures and is only partially developed indicating weak circulation in this vicinity. Comparing with earlier plots in which heat generation is absent (i.e. $\Gamma= 0$ in **Figs. 6a-d to 8a-d**), the presence of a heat source clearly generates multiple cells in each enclosure and intensifies the circulation strength in the vicinity of the upper wall while simultaneously contracting the single cell structure and inducing asymmetric distortions in the streamlines. However, since the Grashof number is much lower in **Figs. 9a-d** (i.e. $Gr=2\times 10^4$) than **Figs. 6a-d to 8a-d** ($Gr=2\times 10^6$) and furthermore magnetic field is four times stronger ($Ha = 20$ here whereas in earlier plots it is 5), the weaker thermal buoyancy and stronger Lorentzian drag force will also contribute to morphing in streamline distributions. The isotherms are much more evenly distributed and approximately parallel to the vertical boundaries for all three enclosure aspect ratios in **Fig. 9b**. With increasing heat generation effect (**Figs. 10b, 11b, 12b**) there is an intensification in isotherm clustering towards the *colder left boundary* which is direct result of the supplementary heat supplied to the circulating fluid, as noted by Gebhart *et al.* [59]. The isotherms however remain essentially vertical in nature. **Fig. 10a** shows that when heat generation is doubled (compared with **Fig. 9b**) i.e. increased to $\Gamma= 2$, a fourth cell emerges in the lower right hand corner of the shallow enclosure ($A = 0.5$) and the primary and secondary cells contract whereas the tertiary cell present also at $\Gamma=1$ (top right corner of enclosure) also expands. However, for the other two enclosure geometries

(tall and square) there remain two basic cells as before although the primary cell is reduced slightly, and the secondary upper cell grows weakly. However, in **Fig. 11b**, it is evident that with further increment in heat generation effect (i.e. $\Gamma = 3$) a tertiary cell begins to synthesize in the tall and square enclosures in the vicinity of the upper right corner which grows with yet further increase in heat generation ($\Gamma = 4$ in **Fig. 12b**). There is also a tendency in **Figs. 11b, 12b** for the quadruple cell structure in the shallow enclosure to become more homogeneously distributed with the fourth cell (lower right corner) growing to a similar magnitude to the primary cell (lower left corner), although there is still asymmetry in the structures, especially in the two upper (secondary and tertiary) cells present in earlier figures. Effectively heat generation which arises in the supplementary term, I/Pr in the energy conservation eqn. (19) serves to supplement the thermal diffusion in the enclosure regime. It is found to have a prominent influence on vortex structure in the enclosures and there is also an intimate interplay with geometry and a noticeable modification in isotherms. **Figs. 13a-b to 16a-b** present the impact of the Grashof number (Gr) on streamline and isotherm distributions. Gr is the key parameter dictating thermal buoyancy effects in the regime and coupling the velocity and temperature fields. It arises in the vorticity momentum eqn. (18) in the spatial temperature gradient term, $+\frac{Gr}{2} \frac{\partial \theta}{\partial x}$. In all the cases studied in **Figs. 13a-b to 16a-b**, $Gr > 10^4$ and this constitutes strong dominance of thermal buoyancy relative to viscous forces in the enclosure. In **fig. 13a, b** at $Gr = 10^4$ (weakest thermal buoyancy case), again dual cell structures are observed in the square and tall enclosures, whereas a triple cell structure is computed for the shallow enclosure. The *primary* cells are however weaker than in earlier plots due to the lower thermal buoyancy effect. Approximately parallel isotherms (vertical) are again generated in all three enclosures, with a stronger clustering towards the left vertical boundary. With a doubling in Grashof number to 2×10^4 (**Figs. 14a, b**), the primary and tertiary cells in the shallow enclosure grow whereas the secondary cell is constricted somewhat. In the tall and square enclosures, the primary cell expands, and the upper secondary cell is observed to contract. Isotherms are more evenly distributed across the enclosure for all three aspect ratios. With subsequent increase in Gr to 2×10^5 (**Fig. 15a, b**) constituting a tenfold rise relative to **Fig. 14a, b**, the *triple cell structure* in the shallow enclosure and *dual vortex structures* in the square and tall enclosures observed at weaker Grashof number, are replaced with a single stronger cell which is generally symmetrical in the square and tall geometries, but is biased towards the left cold vertical wall in the shallow enclosure, rather than the right hot wall. The strength of this single cell is further enhanced with subsequent elevation in Gr to that maximum value simulated (i.e. $Gr = 2 \times 10^6$ in **Figs.**

16a, b) in all three enclosures; however the single cell remains asymmetric in the shallow enclosure, skewed towards the left colder wall and does not extend uniformly across the entire cavity. Although the isotherms in **Fig. 15b** remain basically vertical in nature, they become warped in **Fig. 16b** i.e. they are more clustered towards the upper left corner and lower right corner of the enclosures, and this effect is most pronounced for the shallow enclosure. Clearly the thermal buoyancy effect plays a substantial role in regulating vortex structure and isotherm distribution in the cell and the topologies of the contours demonstrate significant sensitivity to Grashof number. These observations concur with other studies including Wang *et al.* [11] and Stanjnko *et al.* [14] (for non-magnetic Darcian convection in porous media) and Pekemen and Tezer-Sezgin [15] (for Darcian magneto-convection in porous media).

Figs. 17a-b to 19a-b present the impact of increasing Marangoni number (Ma) on streamline and isotherm contour plots for the *square* ($A=1$), *shallow* ($A=0.5$), and *tall* ($A=2$), enclosure cases, respectively.

$Ma = -\frac{\partial \sigma^*}{\partial T} \frac{(T_H - T_C)}{\mu \alpha}$ and is proportional to the temperature

difference between the left cold and right hot walls and inversely proportional to dynamic viscosity and thermal diffusivity. It arises in the surface tension boundary condition in Eqn.

(23), viz, $\Omega = \frac{\partial U}{\partial Y} = -\frac{Ma}{2Pr} \frac{\partial \theta}{\partial x}$. Higher Ma values imply greater surface tension contribution.

This reduces temperatures but increases velocity magnitudes. When Ma is small thermal diffusion dominates whereas for large Ma , Marangoni convection dominates which driven by the gradients in the surface tension (elastic surfacial liquid force). The Marangoni convection currents transport thermal energy, and the Marangoni number compares the rate at which thermal energy is transported by this flow to the rate at which thermal energy diffuses in the boundary layer regime. Inspection of **Fig. 17a, b** shows that for $Ma = 1, 10$ i.e. low surface tension at the upper boundary, a single cell alone is present in the *square enclosure* and isotherms are essentially vertical. With increasing Ma values (20, 50, 100) in **Figs. 17c-e**, a secondary cell however is generated in close proximity to the top left corner and the upper boundary which grows and disperses laterally with stronger surface tension contribution. For $Ma = 20$ this upper secondary cell does not reach the right upper corner; this is only achieved for $Ma = 50$ and 100. Simultaneously the primary lower cell is found to contract as the secondary upper cell expands. A slight clustering effect is also induced in the isotherms towards the left cold wall with greater Marangoni effect, although the topologies remain generally vertical. **Fig. 18a-e** show that for the shallow enclosure, isotherm contours

are generally similar to those computed for the square enclosure. A single cell is also computed at lower Marangoni numbers (**Figs. 18 a, b**); however, the cell does not occupy the entire cavity and is asymmetrically orientated towards the left cold wall. Although this trend is sustained with increment in Marangoni number, a secondary cell appears for $Ma = 20$ (**Fig. 18c**) in the upper left corner and a tertiary cell emerges in the upper right corner. At $Ma = 50$ (**Fig. 18d**), these secondary and tertiary cells grow, the primary cell contracts and a *fourth cell* emerges in the vicinity of the right hot wall and lower right corner. However, at $Ma = 100$ (**Fig. 18e**), this fourth cell vanishes, the secondary cell pushes deeper, and the primary cell is contracted. The tertiary cell also grows significantly along the upper boundary, as a direct consequence of greater surface tension effect. A *shallow enclosure* therefore generates very different internal flow structures in the semiconductor melt with higher Marangoni effect than a square enclosure over the same increment of Marangoni number. Isotherms are also more laterally displaced for the shallow enclosure compared with the square enclosure. **Figs. 19 a-e** indicate that increasing Ma values for the tall enclosure, induce a similar effect to that computed for the square enclosure i.e. the single cell present at low Marangoni number is morphed into a dual cell structure, with a weaker upper secondary cell and a stronger lower primary cell. The vortex structure is inevitably stretched in the vertical direction i.e. taller rather than wider as in the square enclosure case; however, it extends along the *entire upper boundary* in the tall enclosure whereas it is curtailed in the square enclosure. As with the other enclosure aspect ratios in the tall cavity, there is a pronounced clustering of isotherms towards the left cold wall with progressive increase in Marangoni number. Clearly the presence of surface tension at the upper boundary in semiconductor melt processing can be manipulated in conjunction with aspect ratio to achieve considerable modifications in internal thermofluid dynamics of enclosures, which may be beneficial to synthesizing different constitutions of materials manufactured, as noted by Langlois *et al.* [36], among others.

Figs. 20-22 illustrate the distributions in local Nusselt number (Nu) at the right (hot) wall,

computed using Eqn. (24) i.e.
$$Nu = \frac{1}{2} \frac{qH}{k(T_H - T_C)} = -\frac{1}{2} \left[\frac{\partial \theta}{\partial X} \right]_{X=A}$$
. This provides a

quantification for the relative contribution of *thermal convection* to *thermal conduction* contribution at the wall. A very significant decrease in Nu is computed with high Grashof number with distance along the vertical wall (y), as observed in **Fig. 20**. This implies that heat transfer to the wall is strongly suppressed with greater thermal buoyancy effect since thermal diffusion to the enclosure fluid is increased i.e. heat is transported away from the

wall. At lower Grashof numbers, Nusselt number is largely invariant. With increasing Darcy number (Da), **Fig. 21** shows that Nusselt number is markedly boosted i.e. heat transfer to the wall is enhanced with progressively greater permeability. This is attributable to the progressive decrease in presence of solid fibers in the porous medium which manifests in a decrease in thermal conduction between fibers and an elevation in thermal convection to the wall. With progression along the vertical wall from the base to the upper boundary i.e. increasing y values, there is a substantial reduction in Nusselt number. Nusselt numbers are therefore generally greater near the base of the enclosure compared with the upper boundary. Finally, **Fig. 22** indicates that a significant depletion in Nusselt number is induced with increasing Hartmann number, $Ha = \frac{B_0 H \sqrt{\sigma}}{\sqrt{\mu}}$. In all cases the Lorentzian magnetic

body force considerably exceeds the viscous force ($Ha > 5$). With greater magnetic field, increasingly more work must be expended to drag the fluid against the magnetic field. This is dissipated as heat which leads to a boost in temperatures in the enclosure. Therefore, heating is induced within the enclosure and cooling generated at the walls, resulting in a depletion in Nusselt numbers. This is a classical result in magnetohydrodynamic convection, as noted by Cramer and Pai [53] among others. Peak Nusselt numbers arise near the base of the right wall and are systematically reduced with progression upwards along the wall i.e. y coordinate values, plummeting to a minimum at the upper boundary.

6. CONCLUSIONS

Marangoni thermo-convection flow of an electrically conducting Newtonian fluid in an isotropic porous rectangular semiconductor melt enclosure with buoyancy and internal heat generation effects, has been studied in this article. Darcy's model has been employed to simulate porous medium drag in the viscous-dominated regime. The governing equations comprising the mass conservation, x -direction momentum, y -direction momentum and energy equation have been presented with a quartet of boundary conditions at the four walls of the enclosure. The upper enclosure wall is assumed to be "free" with an appropriate surface tension dynamic boundary condition for thermo-capillary (Marangoni) convection. The boundary value problem has been rendered into vorticity-stream function form with appropriate transformations. An efficient marker-and cell (MAC) numerical finite difference method has been utilized to solve the boundary value problem with physically realistic data of relevance to semiconductor melts. Validations with earlier purely fluid solutions (*infinite*

Darcy number) have been conducted. A detailed parametric study of the influence of Marangoni number (Ma), Grashof number (Gr), Darcy number (Da) and internal heat generation parameter (I) on streamline and isotherm contours has been conducted for three different aspect ratios (shallow, tall and square enclosures) with Prandtl number (Pr) equal to 0.054. Local Nusselt numbers at the right (hot) wall are also computed for the influence of Hartmann hydromagnetic number (Ha), Grashof number (Gr) and Darcy number (Da). The simulations have shown that:

(i) A substantial reduction in local Nusselt number at the right (hot) wall is produced with stronger magnetic field (greater Hartmann number) and Grashof number whereas it is enhanced with greater Darcy number.

(ii) With increasing *Marangoni effect*, the single cell present in square and tall enclosures is morphed into a dual cell structure, with a weaker upper secondary cell and a stronger lower primary cell. However, a four-cell structure is computed in the shallow enclosure with increasing Marangoni number i.e. stronger surface tension effect at the upper boundary.

(iii) For all three enclosures (shallow, square and tall), there is greater clustering of isotherms towards the left cold wall with increment in Marangoni number.

(iv) With greater heat generation effect a tertiary cell is generated in the tall and square enclosures in the vicinity of the upper right corner which continues to expand. Furthermore, the quadruple cell structure in the shallow enclosure becomes increasingly symmetric with stronger heat source effect.

(v) With a large increase in Grashof number, the *triple vortex structure* in the shallow enclosure and *dual vortex structures* in the square and tall enclosures observed at weaker Grashof number, morph into a *single stronger vortex* which is generally symmetrical in the square and tall geometries; however this single cell is orientated more strongly towards the left cold vertical wall in the shallow enclosure, rather than the right hot wall.

(vi) For the shallow enclosure, with increasing Darcy number (i.e. higher permeability of the porous medium), streamlines become distorted and evolve into an asymmetric distribution biased towards the left cold wall boundary and a single trapped cell is computed. The isotherms are increasingly clustered towards the right wall.

(vii) In the tall enclosure, an increment in Darcy number (Da) leads to a weaker distortion in isovels (streamlines) towards the upper left corner and lower right corner of the enclosure, with considerable elongation in the vertical direction is induced. Isotherms are also observed

to become increasingly sigmoidal in nature and biased more towards the top left and base wall than for the square enclosure, although less so than for the shallow enclosure.

The present model which finds applications in the electromagnetic control of semiconductors, has been confined to the Darcian porous medium case with a horizontal magnetic field. Future studies will investigate the influence on non-Darcy (e.g. *Forchheimer* quadratic drag) [60] and *oblique* magnetic field effects [61] and will be communicated soon.

REFERENCES

- [1] A. Bairi *et al.*, A review on natural convection in enclosures for engineering applications. The particular case of the parallelogrammic diode cavity, *Applied Thermal Engineering*, 63 (1), 304-322 (2014).
- [2] Robillard, L., Vasseur, P. and Nguyen, T.H., Thermoconvective heat transfer in a rectangular cavity with constant cooling rate, *Int. Conf. Numerical Methods in Laminar and Turbulent Flow, Vencie, Italy*, 113-119, July (1981).
- [3] Kwak, H.S. and Hyun, J.M., Natural convection in an enclosure having a vertical sidewall with time-varying temperature, *J. Fluid Mechanics*, 329, 65-85 (1996).
- [4] Bennacer. R, Mohamad A.A, Akrou D., Transient natural convection in an enclosure with horizontal temperature and vertical solutal gradients, *Int. J. Thermal Sci.*, 40, 899–910 (2001).
- [5] H. Welhezi *et al.*, Numerical analysis of natural convection between a heated cube and its spherical enclosure, *International Journal of Thermal Sciences*, 150, 105828 (2020).
- [6] R. Bhargava, S. Sharma, P. Bhargava, O. Anwar Bég and A. Kadir, Finite element simulation of nonlinear convective heat and mass transfer in a micropolar fluid-filled enclosure with Rayleigh number effects, *Int. J. Applied Computational Mathematics*, 3 (2), 1347–1379 (2017).
- [7] S. Kuharat, O. Anwar Bég, Ali Kadir, Computational fluid dynamic simulation of a solar enclosure with radiative flux and different metallic nano-particles, *International Conference on Innovative Applied Energy (IAPE'19), Oxford, United Kingdom, 14-15 March* (2019).
- [8] A.Y. Gelfgat, P.Z. Bar-Yoseph, Effect of an external magnetic field on oscillatory instability of convective flows in rectangular cavity, *Phys. Fluids*, 13 (2001) 2269–2278.
- [9] G.C. Bourantas and V.C. Loukopoulos, MHD natural-convection flow in an inclined square enclosure filled with a micropolar-nanofluid, *International Journal of Heat and Mass Transfer*, 79, 930-944 (2014).
- [10] M.A. Sheremet *et al.*, MHD natural convection in an inclined wavy cavity with corner heater filled with a nanofluid, *Journal of Magnetism and Magnetic Materials*, 416, 37-47 (2016).
- [11] Wang, C.H., Vasseur, P., Robillard, L., Natural convection in a confined porous medium, *11th Canadian Congress of Applied Mechanics*, 132-134 (1987).
- [12] Amahmid, A., Hasnaoui, M. and Vasseur, P., Double-diffusive natural convection in a vertical enclosure filled with porous medium, *Int. Conf. Fluidic Thermal Energy Conversion, Jakarta, Indonesia*, 487-492 (1997).

- [13] C. Zhang *et al.*, A mixed finite element solver for natural convection in porous media using automated solution techniques, *Computers & Geosciences*, 96, 181-192 (2016).
- [14] J. K. Stajanko, Simulation of natural convection in porous media by boundary element method, *Numerical Simulations in Engineering and Science*, Ed. S. Rao, Intech Open (2020).
- [15] B. Pekemen and M. Tezer-Sezgin, DRBEM solution of free convection in porous enclosures under the effect of a magnetic field, *International Journal of Heat and Mass Transfer*, 56, 454-468 (2013).
- [16] Alchaar, S., Vasseur, P. and Bilgen, E., Effect of an electromagnetic field on natural convection in a porous medium, *7th Int. Symp. Transport Phenomena in Manufacturing Processes, Acapulco, Mexico*, 275-280 (1994).
- [17] A.I. Alsabery *et al.*, Effects of viscous dissipation and radiation on MHD natural convection in oblique porous cavity with constant heat flux, *Advances in Applied Mathematics and Mechanics*, 9, 463-484 (2017).
- [18] B. Pekemen and M. Tezer-Sezgin, MHD flow and heat transfer in a lid-driven porous enclosure, *Computers & Fluids*, 89, 191-199 (2014).
- [19] O. Anwar Bég, Lik Sim, J. Zueco and R. Bhargava, Numerical study of magnetohydrodynamic viscous plasma flow in rotating porous media with Hall currents and inclined magnetic field influence, *Communications in Nonlinear Science and Numerical Simulation*, 15, 345-359 (2010).
- [20] M.M. Bhatti, C.M. Khaliq, Tasveer Bég, O. Anwar Bég and Ali Kadir, Numerical study of slip and radiative effects on magnetic Fe₃O₄-water-based nanofluid flow from a nonlinear stretching sheet in porous media with Soret and Dufour diffusion, *Modern Physics Letters B* 33, 2050026 (24 pages) (2020).
- [21] Muralidhar, K. and Kulacki, F.A., Non-Darcy natural convection in a saturated horizontal porous annulus, *ASME J. Heat Transfer*, 110, 133-139 (1988).
- [22] Shivakumara, I.S., Prasanna, B.M.R., Rudraiah, N. and Venkatachalappa, M., Numerical study of natural convection in a vertical cylindrical annulus using a non-Darcy equation, *J. Porous Media*, 5, 2, (2002).
- [23] Khadrawi, A.F. and Nimr, M.A., The effect of the local inertia term on the free convection fluid flow in a vertical channel partially filled with porous media, *J. Porous Media*, 6, 59-70 (2003).
- [24] S. Rawat, R. Bhargava, Renu Bhargava and O. Anwar Bég, Transient magneto-micropolar free convection heat and mass transfer through a non-Darcy porous medium channel with variable thermal conductivity and heat source effects, *Proc. IMechE. Part C- J. Mechanical Engineering Science*, 223, 2341-2355 (2009).
- [25] V. R. Prasad, B. Vasu and O. Anwar Bég, Thermo-diffusion and diffusion-thermo effects on free convection flow past a horizontal circular cylinder in a non-Darcy porous medium, *J. Porous Media*, 16, 4, 315-334 (2013).
- [26] V.R. Prasad, S. A. Gaffar and O. Anwar Bég, Non-similar computational solutions for free convection boundary-layer flow of a nanofluid from an isothermal sphere in a non-Darcy porous medium, *J. Nanofluids*, 4, 1-11 (2015).

- [27] A.M. Aly, Double-diffusive natural convection in an enclosure including/excluding sloshing rod using a stabilized ISPH method, *International Communications in Heat and Mass Transfer*, 73, 84-99 (2016).
- [28] O. Anwar Bég, N. Ali, A. Zaman, Eemaan T. A. Bég and Ayesha Sohail, Computational modelling of heat transfer in annular porous medium solar energy absorber with a P1-radiative differential approximation, *J. Taiwan Inst. Chemical Eng.*, 66, 258-268 (2016).
- [29] M. Dreyer, Propellant behaviour in launcher tanks: an overview of the COMPERE program, *Progress in Propulsion Physics*, 1, 253-266 (2009).
- [30] S. Yamamoto, M. Kikuchi, S. Yoda, M. Mikami, Effect of Marangoni convection on flame spread of a fuel droplet array, *43rd AIAA Aerospace Sciences Meeting and Exhibit, Nevada, USA* (2005).
- [31] O. Zikanov *et al.*, A model for thermal Marangoni drying, *Journal of Engineering Mathematics*, 40, 249–267 (2001).
- [32] T.D. Bennett, Marangoni mechanism in pulsed laser texturing of magnetic disk substrates, *ASME J. Heat Transfer*, 119(3): 589–596 (1997).
- [33] J.-M. Drezet, S. Pellerin, C. Bezençon and S. Mokadem, Modelling the Marangoni convection in laser heat treatment, *J. Phys. IV France*, 120, 299-306 (2004).
- [34] D. Camel, P. Tison, J.J. Favier, Marangoni flow regimes in liquid metals, *Acta Astronautica*, 13, 723-726 (1986).
- [35] D. Schwabe, A. Scharmann, Microgravity experiments on the transition from laminar to oscillatory thermocapillary convection in floating zones, *Adv. Space Research*, 4, 43-47 (1984).
- [36] Langlois, W. E. *et al*, Effects of the finite electrical conductivity of the crystal on hydromagnetic Czochralski flow, *Journal of Crystal Growth*, 83, 51-61 (1987).
- [37] D. R. Sastry *et al.* The effect of heat transfer on MHD Marangoni boundary layer flow past a flat plate in nanofluid, *International Journal of Engineering Mathematics*, Volume 2013, Article ID 581507, 6 pages (2013).
- [38] J. Zueco and O. Anwar Bég, Network numerical simulation of hydromagnetic Marangoni mixed convection boundary layers, *Chemical Engineering Communications*, 198, 4, 552-571 (2010).
- [39] Zhang, Y. *et al.* Analysis of MHD thermosolutal Marangoni convection with the heat generation and a first-order chemical reaction, *Chem. Eng. Sci.* 69, 449-455 (2012).
- [40] O. Anwar Bég, M. Ferdows, Shamima Islam and M. Nazrul Islam, Numerical simulation of Marangoni magnetohydrodynamic bio-nanofluid convection from a non-isothermal surface with magnetic induction effects: a bio-nanomaterial manufacturing transport model, *J. Mechanics Medicine Biology*, 14, 3, 1450039.1-1450039.32 (2014).
- [41] Y. Lin *et al.*, Magnetohydrodynamics thermocapillary Marangoni convection heat transfer of power-law fluids driven by temperature gradient, *ASME J. Heat Transfer*. 135(5): 051702 (2013).

- [42] N. Ma *et al.*, Forced convection during liquid encapsulated crystal growth with an axial magnetic field, *ASME J. Fluids Eng.* 120(4): 844-850 (1998).
- [43] N. Rudraiah *et al.*, Combined surface tension and buoyancy-driven convection in a rectangular open cavity in the presence of a magnetic field, *International Journal of Non-Linear Mechanics*, 30, 759-770 (1995).
- [44] Chippada, S., Jue, T.C. and Ramaswamy, B., Finite element simulation of combined buoyancy and thermocapillary driven convection in open cavities, *Int. J. Numerical Methods in Engineering*, 38, 335-351 (1995).
- [45] Saghir, M.Z., Hennenberg, M., Legros, J.C. and Islam, M.R., Rayleigh-Marangoni convection in a porous cavity, *Int. Symp. Advances in Computational Heat Mass Transfer, 26-30 May, CESME, Turkey* (1997).
- [46] Juel, A., Mullin, T., Ben Hadid, H. and Henry, D., Magneto hydrodynamic convection in molten gallium, *J. Fluid Mechanics*, 378, 97-118 (1999).
- [47] M. Saleem *et al.*, Double diffusive Marangoni convection flow of electrically conducting fluid in a square cavity with chemical reaction, *ASME J. Heat Transfer*, 136(6): 062001 (2014).
- [48] M. A. Hossain, M.Z. Hafiz, D.A.S. Rees, Buoyancy and thermocapillary driven convection flow of an electrically conducting fluid in an enclosure with heat generation, *International Journal of Thermal Sciences*, 44, 676–684 (2005).
- [49] O. Anwar Bég, J. Zueco, Bég, T.A., H.S. Takhar, and E. Kahya, NSM analysis of time-dependent nonlinear buoyancy-driven double-diffusive radiative convection flow in non-Darcy geological porous media, *Acta Mechanica*, 202, 181-204 (2009).
- [50] O. Anwar Bég and O.D. Makinde, Viscoelastic flow and species transfer in a Darcian high-permeability channel, *Petroleum Science and Engineering*, 76, 93–99 (2011).
- [51] O. Anwar Bég, B. Islam, MD. Shamshuddin and T. A. Bég, Computational fluid dynamics analysis of moisture ingress in aircraft structural composite materials, *Arabian J. Science Engineering* (2019). doi.org/10.1007/s13369-019-03917-4 (23 pages)
- [52] F.H. Harlow, The marker-and-cell method, *Numerical Methods in Fluid Dynamics, Von Karman Inst. for Fluid Dynamics, Belgium*, 38 pp. (1972).
- [53] K.C. Cramer and S. I. Pai, *Applied Magnetofluid Dynamics for Engineers and Applied Physicists*, MacGraw-Hill, New York, New York, USA (1973).
- [54] D. de Vahl Davis, Natural convection of air in a square cavity: a benchmark solution, *Int. J. Num. Meth. Fluids*, 3, 249-264 (1983).
- [55] M. T. Manzari, An explicit finite element algorithm for convective heat transfer problems, *Int. J. Numer. Meth. Heat Fluid Flow*, 9, 860- 877 (1999).
- [56] D. C. Wan, B. S. V. Patnaik, and G. W. Wei, A new benchmark quality solution for the buoyancy-driven cavity by discrete singular convolution, *Numerical Heat Transfer: Part B*, 40: 199-228 (2001).

- [57] K. Venkatadri, S. Abdul Gaffar, V. R. Prasad, B. Md. Hidayathualla Khan and O. Anwar Bég, Simulation of natural convection heat transfer in a 2-D trapezoidal enclosure, *International Journal of Automotive and Mechanical Engineering*, 16 (4) 7375-7390 (2019).
- [58] K. Venkatadri, O. Anwar Bég, V. R. Prasad, Numerical simulation of thermal radiation influence on natural convection in a trapezoidal enclosure: heat flow visualization through energy flux vectors, *Int. J. Mechanical Sciences*, 171 (2020). doi.org/10.1016/j.ijmecsci.2019.105391 (9 pages)
- [59] B. Gebhart *et al.*, *Buoyancy-induced Flows and Transport*, Hemisphere, Washington, USA (1988).
- [60] J.C. Umavathi and O. Anwar Bég, Numerical study of double-diffusive dissipative reactive convective flow in an open vertical duct containing a non-Darcy porous medium with Robin boundary conditions, *J. Engineering Mathematics* (2019). <https://doi.org/10.1007/s10665-019-10022-w> (13 pages)
- [61] O. Anwar Bég, S.K. Ghosh and M. Narahari, Mathematical modelling of oscillatory MHD Couette flow in a rotating highly permeable medium permeated by an oblique magnetic field, *Chemical Engineering Communications*, 198, 235-254 (2010).
- [62] **GAMM Workshop on Numerical Simulation of Oscillatory Convection in Low Prandtl Number Fluids.** Marseille, 1988, Proceedings to appear in *Notes on Numerical Fluid*.
- [63] **B. ROUX** and H. BEN HADID, Numerical Simulation of Oscillatory Convection In Semiconductor Melts, *Journal of Crystal Growth* 97 (1989) 201—216.
- [64] Y.S. Tian, T.G. Karayiannis, Low turbulence natural convection in an air filled square cavity Part I: the thermal and fluid flow fields, *International Journal of Heat and Mass Transfer* 43 (2000) 849-866.
-